ANT2 Accelerates Cutaneous Wound Healing in Aged Skin by Regulating Energy Homeostasis and Inflammation

JID Open

Seung-Hwa Woo[1], Yun Jeong Mo[2], Yun-Il Lee[2], Ji Hwan Park[1], Daehee Hwang[3], Tae Jun Park[4,5], Hee Young Kang[5,6], Sang Chul Park[7] and Young-Sam Lee[1,2]

An effective healing response is critical to healthy aging. In particular, energy homeostasis has become increasingly recognized as a factor in effective skin regeneration. ANT2 is a mediator of adenosine triphosphate import into mitochondria for energy homeostasis. Although energy homeostasis and mitochondrial integrity are critical for wound healing, the role played by ANT2 in the repair process had not been elucidated to date. In our study, we found that ANT2 expression decreased in aged skin and cellular senescence. Interestingly, overexpression of ANT2 in aged mouse skin accelerated the healing of full-thickness cutaneous wounds. In addition, upregulation of ANT2 in replicative senescent human diploid dermal fibroblasts induced their proliferation and migration, which are critical processes in wound healing. Regarding energy homeostasis, ANT2 overexpression increased the adenosine triphosphate production rate by activating glycolysis and induced mitophagy. Notably, ANT2-mediated upregulation of HSPA6 in aged human diploid dermal fibroblasts downregulated proinflammatory genes that mediate cellular senescence and mitochondrial damage. This study shows a previously uncharacterized physiological role of ANT2 in skin wound healing by regulating cell proliferation, energy homeostasis, and inflammation. Thus, our study links energy metabolism to skin homeostasis and reports, to the best of our knowledge, a previously unreported genetic factor that enhances wound healing in an aging model.

Journal of Investigative Dermatology (2023) **143,** 2295–2310; doi:10.1016/j.jid.2023.05.002

INTRODUCTION

The skin forms a protective barrier against external stress (Harris-Tryon and Grice, 2022) and is composed of multiple layers that cooperate through intrinsic and extrinsic signaling for maintaining tissue homeostasis (Mintie et al., 2020). Wound healing is a regeneration process with a tightly regulated sequence of biochemical events. These biochemical events are classified into the following four phases: blood clotting (hemostasis), inflammation, tissue growth (proliferation), and tissue remodeling (extracellular cellular matrix maturation) (Stadelmann et al., 1998). A disruption to any of these phases leads to unhealed wounds, especially in diabetes, venous or arterial disease, infection, and metabolic deficiencies associated with old age (Ellis et al., 2018). Therefore, it is a prerequisite to the understanding of how wound healing phases are regulated and to identifying the critical factors to restore the protective barrier.

Inevitably, wound healing decelerates with age, which is accompanied by a gradual decline in tissue integrity and function, including delayed epithelialization and granulation tissue formation (Ding et al., 2021). In the wound healing process, fibroblasts are primary cells critical for all the general phases, such as transforming responses from the acute inflammatory state to adaptive immunity and initiating angiogenesis, epithelialization, and collagen formation (Bainbridge, 2013; Buckley et al., 2001; Reinke and Sorg, 2012; Virag et al., 2007). In particular, dermal fibroblasts in aging skin are characterized by loss of proliferation and decreased synthesis of dermal extracellular matrix components, which are critical to skin homeostasis and regeneration (Zhai et al., 2021). Although the molecular and cellular factors underlying the healing ability of aged skin remain elusive, functional restoration of dermal fibroblasts in aged skin would be assumed to facilitate the effective wound healing response.

Proper regulation of energy metabolism is essential for wound healing. With increasing age, adenosine triphosphate (ATP) production is decreased because of accumulated

[1]*Department of New Biology, Daegu Gyeongbuk Institute of Science and Technology (DGIST), Daegu, Republic of Korea;* [2]*Well Aging Research Center, Division of Biotechnology, Daegu Gyeongbuk Institute of Science and Technology (DGIST), Daegu, Republic of Korea;* [3]*Department of Biological Sciences, Seoul National University, Seoul, Republic of Korea;* [4]*Department of Biochemistry and Molecular Biology, Ajou University School of Medicine, Suwon, Republic of Korea;* [5]*Institution of Inflammaging Translational Research Center, Ajou University School of Medicine, Suwon, Republic of Korea;* [6]*Department of Dermatology, Ajou University School of Medicine, Suwon, Republic of Korea; and* [7]*The Future Life & Society Research Center, Advanced Institute of Aging Science, Chonnam National University, Gwangju, Republic of Korea*

**Correspondence: Young-Sam Lee, Department of New Biology, Daegu Gyeongbuk Institute of Science and Technology (DGIST), 333 Technojungang-Daero, Hyeonpung-Eup, Dalsung-Gun, Daegu 42988, Republic of Korea. E-mail: lee.youngsam@dgist.ac.kr*

Abbreviations: ANT2-OE, ANT2-overexpressing; ATP, adenosine triphosphate; ECAR, extracellular acidification rate; HDF, human dermal fibroblasts; mCherry-OE, mCherry-overexpressing; RNA-seq, RNA-sequencing

Received 24 October 2022; revised 26 April 2023; accepted 5 May 2023; accepted manuscript published online 20 May 2023; corrected proof published online 15 June 2023

dysfunctional mitochondria and impaired mitochondrial quality control (Chistiakov et al., 2014). Meanwhile, glycolysis compensates for a critical reduction in ATP generation in aged skin (Prahl et al., 2008; Ravera et al., 2019; Schniertshauer et al., 2018). An increased energy supply enables cellular restoration and tissue damage repair. Interestingly, the wound healing process is preferentially advanced through glycolysis, which prevents excessive ROS production and quickly replenishes energy. ATP and glycolytic intermediates are necessary for macrophage and neutrophil function during the inflammatory phase of wound healing (Caputa et al., 2019; Soto-Heredero et al., 2020). In addition, increased lactate concentrations under inflammatory conditions initiate signals for angiogenesis, connective tissue deposition, and collagen synthesis (Beckert et al., 2006; Lee, 2021). However, the modulation of metabolic properties for effective wound healing in older adult individuals has been largely unexplored.

ANT2 is a mitochondrial translocator, which imports glycolytic ATP into the mitochondrial matrix when oxidative phosphorylation is impaired to meet the energy demand, which maintains the mitochondrial membrane potential and mitochondrial energy homeostasis and promotes cell survival in cancer (Pak et al., 2013; Pan et al., 2020). In particular, ANT2 is mainly expressed in proliferative and undifferentiated cells, and its expression is reduced in aged cells (Chevrollier et al., 2011). Notably, ANT2 expression is regulated by proinflammatory cytokine pathways, including IFN-γ and TNF-α pathways, which are involved in cellular senescence through the TGFβ/SMAD pathway (Hubackova et al., 2016). Although many key functions of ANT2 have been characterized, whether ANT2 contributes to wound healing by regulating energy metabolism and cellular homeostasis in aged skin remains unknown.

In this study, we showed that ANT2 overexpression enhanced wound healing in aged skin, particularly enhancing proliferation by shifting energy metabolism to glycolysis and alleviating proinflammatory condition by upregulating HSP70. Collectively, our data suggest that ANT2 could be, to the best of our knowledge, a previously unreported therapeutic target for skin wound healing during aging by compensating for the loss of cell function throughout the lifespan.

RESULTS

ANT2 expression is downregulated in aged skin

To investigate the relationship between mitochondrial energy homeostasis and skin maintenance during aging, we first examined the expression of the adenine nucleotide translocase genes in human aging. In the adenine nucleotide translocase family, ANT2 is a major protein abundant in the skin (Supplementary Figure S1a), according to the analysis of a transcriptome dataset of cultured human dermal fibroblasts (HDFs) from people aged between 1 and 94 years (Fleischer et al., 2018). Interestingly, ANT2 expression was significantly decreased with age (Supplementary Figure S1b). We also analyzed a recently published single-cell RNA-sequencing (RNA-seq) dataset of human skin samples from four elderly (aged >60 years) and three young (aged <30 years) females (Ahlers et al., 2022). We identified 66,201 fibroblasts belonging to six clusters (0, 1, 2, 3, 8, and 10), which were confirmed by the expression of the fibroblast markers (*COL1A2*, *DCN*, and *LUM*) used in this study (Supplementary Figure S1c). Among the six fibroblast clusters, *ANT2* transcript was significantly downregulated in the reticular cluster, expressing *SLPI* (cluster 1), and the mesenchymal cluster, expressing *ASPN* (cluster 10) (Supplementary Figure S1d and e). Immunohistochemical staining targeting ANT2 in human skin confirmed the reduced expression level of ANT2 in the dermal layer of aged skin (Supplementary Figure S1f). Moreover, the ANT2 protein level was reduced in replicative senescent HDFs (Supplementary Figure S1g). Similarly, *Ant2* showed patterns of gradually decreasing expression during mouse aging, as indicated by previous analysis of a transcript database of mouse skin (GSE75192) (Aramillo Irizar et al., 2018) (Supplementary Figure S1h). Consistent with these results, ANT2 protein abundance was found to decrease in mouse skin in an age-dependent manner (Supplementary Figure S1i). Taken together, these data suggest that ANT2 is associated with the impairment of skin homeostasis in older adult individuals and can be considered a potential therapeutic target to treat skin aging.

ANT2 alleviates senescent phenotypes of HDFs

ANT2 is expressed in rapidly growing cells (Jang et al., 2008). As shown in our data, ANT2 expression downregulates on aging; therefore, we hypothesized that the overexpression of ANT2 in a cultured replicative senescent HDF population would induce cell proliferation. As expected, ANT2 overexpression in senescent HDFs (i.e., ANT2-overexpressing [ANT2-OE] cells) significantly increased pH3S10, a cell proliferation marker, along with the decreased expression of p16 and p21, which are involved in cell cycle arrest (Coppé et al., 2011; Stuhldreier et al., 2015; Tubita et al., 2022) (Figure 1a). Consistently, ANT2-OE cells showed a significantly increased 5-ethynyl-20-deoxyuridine incorporation compared with the mCherry-overexpressing (mCherry-OE) senescent HDFs (i.e., mCherry-OE cells) (Figure 1b and c). To test whether ANT2 overexpression may induce cell death in severely damaged senescent cells by apoptosis, we monitored the activation of caspases involved in the intrinsic apoptosis pathway. The results showed that caspase-9 and -3 were activated in the ANT2-OE cells, but caspase-7 was not activated (Supplementary Figure S2). Notably, caspase-7 was the primary executor in apoptosis that affected cell viability (Lakhani et al., 2006). In addition, activation of caspases is also associated with non-apoptotic processes, including the regulation of mitochondrial homeostasis by caspase-9 (An et al., 2020) and the regulation of cell proliferation and size by caspase-3 (Yosefzon et al., 2018). Collectively, these results indicate that ANT2 overexpression may trigger cell proliferation, although ANT2-induced apoptosis in senescent cells cannot be ruled out because caspase-3 is also regarded as an executioner caspase capable of inducing apoptosis upon activation. During cellular senescence, morphological changes, including increased cell size and granularity and accumulation of lipofuscin, an undegradable autofluorescent age pigment, are accompanied by cell-cycle arrest (Bertolo et al., 2019; Passos and von Zglinicki, 2007). Interestingly, ANT2 overexpression exhibited reduced forward scatter (indicative of relative cell size), side scatter (indicative of the subcellular organelle granularity), and autofluorescence compared with mCherry overexpression (Figure 1d and e). These data indicate that ANT2 triggers the

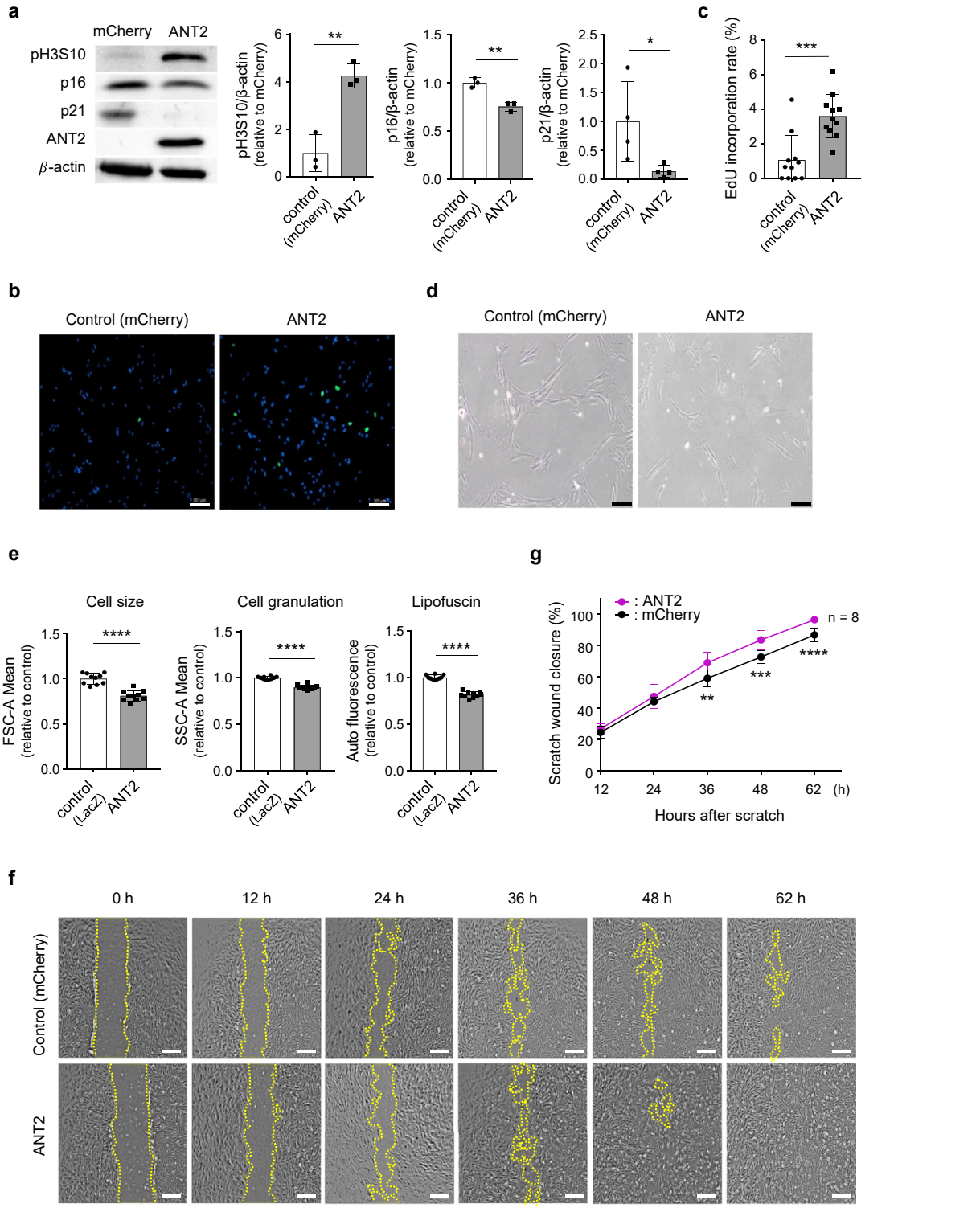

Figure 1. Effect of ANT2 overexpression on alleviating senescent phenotypes in HDFs. (**a**) Immunoblots and quantification of pH3S10 and p16 and p21 protein expression in mCherry-OE (control) and ANT2-OE senescent HDFs. β-Actin was used for normalization. The data are shown as the mean ± SD; n (biological replicate) = 3–4. (**b, c**) Images and quantification of EdU incorporation in mCherry-OE (control) and ANT2-OE senescent HDFs. The data are shown as the mean ± SD; n (view field) = 11. (**d, e**) Changes in cell morphology after transduction in senescent HDFs. Representative images showing the cell morphology (**d**) and measurement of cellular features as indicated by flow cytometry (**e**). The data are shown as the mean ± SD; n (biological replicate) = 10. (**f, g**) Time-lapse images of wound closure in the mCherry-OE (control) and ANT2-OE senescent HDF monolayers 0, 12, 24, 36, 48, and 62 hours after scratching. The cell migration terminal region is indicated by a yellow dotted line. Bar = 500 μm. The migration area was quantified using ImageJ software. The data are shown as the mean ± SD; n (biological replicate) = 8. For statistical analyses in **a**–**g**, $^{*}P \leq 0.05$, $^{**}P \leq 0.01$, $^{***}P \leq 0.001$, and $^{****}P \leq 0.0001$ as determined by unpaired *t*-test. ANT2-OE, ANT2-overexpressing; EdU, 5-ethynyl-20-deoxyuridine; FSC-A, forward scatter area; h, hour; HDF, human dermal fibroblast; mCherry-OE, mCherry-overexpressing; SSC-A, side scatter area.

alleviation of key features observed in senescent cell populations, although the effect may be limited to the pre or early-senescent cells in the population.

The cell cycle directly affects cell proliferation and migration (Boehm and Nabel, 2001). Because collective cell migration is considered a hallmark of wound repair (Grada et al., 2017), we next examined the cell migratory ability after ANT2 overexpression by performing a scratch assay. Consistent with the facilitated wound repair induced by ANT2 overexpression in aged mouse skin, the ANT2-OE cell monolayer showed faster scratch closure than the mCherry-OE cell monolayer (control) (Figure 1f and g). Taken together, these results suggest that ANT2 overexpression induces a beneficial effect in wound healing in part by alleviating senescence phenotypes of HDFs.

ANT2 overexpression accelerates in vivo wound healing in aged skin

To determine whether enhanced ANT2 expression plays a beneficial role in the homeostasis of aged skin, we tested the effect of ANT2 overexpression on wound healing in aged skin (Figure 2a). Mice were randomly assigned to two groups: a control (mCherry-OE; mCherry) group and an ANT2-OE (ANT2) group. Lentiviral particles overexpressing each of the corresponding genes (Supplementary Figure S3a and b) were subcutaneously injected into the mouse dorsal skin. Four days after the injection, a full-thickness cutaneous wound (6 mm in diameter) was made on the injection sites, and time-dependent wound closure was measured. No erythema, edema, or irritation was observed at the wound site in either the mCherry (control) or ANT2 group (Figure 2b). As expected, ANT2 induced a significant promotion of wound healing on days 10 and 14 (Figure 2b and c) with a reduced granulation in the wound site observed by H&E and Masson's trichrome staining (Figure 2d) (Braiman-Wiksman et al., 2007).

Next, we evaluated the effect of ANT2 in each phase of wound healing by performing histological analyses. Compared with the mCherry group (control), the ANT2 group exhibited a reduced number of F4/80- and Ly6G-positive cells, representing macrophages and neutrophils, respectively, in the wound site on day 3 (inflammatory phase) (Figure 2e). On days 7−14 (proliferation phase), the ANT2 group exhibited an increased number of Ki-67−positive cells (Figure 2f and g), representing proliferating cells. Moreover, cells expressing CD31, a major angiogenesis marker, were significantly recruited to wound healing sites in the ANT2 group on day 14 (Figure 2g). Supplementing data mentioned earlier, result of H&E staining showed that there were more regular cells (mononuclear) than immune cells (multinuclear) in the ANT2 group from day 3 to day 14 (Supplementary Figure S4a−d). Thus, these data support the idea that ANT2 expression in the dermis promotes wound healing in aged mice by modulating the degree of inflammation and inducing cell proliferation and angiogenesis.

ANT2 improves ATP production by upregulating glycolysis in aging

ANT2 plays an important role in cellular energy metabolism. In particular, it maintains the mitochondrial membrane potential by importing glycolytic ATP into the mitochondrial matrix (Chevrollier et al., 2011). However, it is unclear how metabolic process is altered and what is the beneficial effect after acquiring ATP by ANT2. Therefore, we examined real-time energy metabolism by measuring the extracellular acidification rate (ECAR), oxygen consumption rate, and proton efflux rate after ANT2 overexpression in senescent HDFs. The ECAR levels for basal glycolysis, glycolytic capacity, and glycolytic reserve in the ANT2-OE cells were significantly higher than those in the mCherry-OE cells (control) in the glycolysis stress test, indicating that the ANT2-OE cells showed increased glycolysis compared with the control group (Figure 3a). Meanwhile, ANT2-OE cells exhibited marginally increased basal respiration, and the maximal respiration and spare respiration capacity were decreased in a mitostress test, compared with those in the control cells (Supplementary Figure S5a). In the proton efflux rate analysis, ANT2-OE cells showed significantly increased total ATP production, depending on glycolysis (Figure 3b). These data suggest that the energy dependency of ANT2-OE cells shifts toward glycolysis to accommodate the energy demand for increased cell proliferation.

To investigate the detailed glycolysis-related energy metabolic flux in the ANT2-OE senescent HDFs, we examined the levels of the key glycolytic metabolites, including lactate and pyruvate. Consistent with the shift toward glycolysis by ANT2 overexpression, the lactate level was elevated in ANT2-OE cells, compared with that in mCherry-OE cells (Figure 3c). However, the pyruvate level was not changed by ANT2 overexpression (Figure 3d). Because pyruvate fuels the tricarboxylic acid cycle, we assessed the activity of pyruvate dehydrogenase by monitoring the phosphorylation of pyruvate dehydrogenase at Ser293. Interestingly, the phosphorylation of pyruvate dehydrogenase was reduced in the ANT2-OE cells (Supplementary Figure S5b), which indicated that the tricarboxylic acid cycle would be activated in the condition. Furthermore, the ratio of NAD^+/NADH was reduced, along with elevated NADH level (Figure 3e), which supports the activation of the tricarboxylic acid cycle by ANT2 overexpression in senescent HDFs.

Next, we assessed cell migration on the basis of the glycolytic rate to determine whether the increased glycolytic ATP production due to ANT2 overexpression contributed to wound healing. In the presence of sodium oxamate, a competitive inhibitor of lactate dehydrogenase as a structural analog of pyruvate (Seliger et al., 2014), which significantly inhibited glycolytic capacity at concentrations >10 mM in senescent HDFs (Supplementary Figure S6a), the cell migration rate was significantly reduced in both the ANT2-OE cells and mCherry-OE cells (control) (Supplementary Figure S6b). Collectively, our data show that ANT2 overexpression increased glycolytic ATP production, which suggests that ANT2 induction during aging can reprogram the energy metabolism to promote wound healing.

ANT2 overexpression enhances the removal of damaged mitochondria in aging

Mitochondrial turnover and function are closely related to mitochondrial morphology, which has been reported to be an aging marker in various tissues (Kataoka et al., 2020). Therefore, we observed the mitochondrial morphology after ANT2 overexpression. ANT2-OE cells showed smaller and more compact mitochondria (Figure 4a−c). In contrast, LacZ-overexpressing control cells showed elongated and interconnected

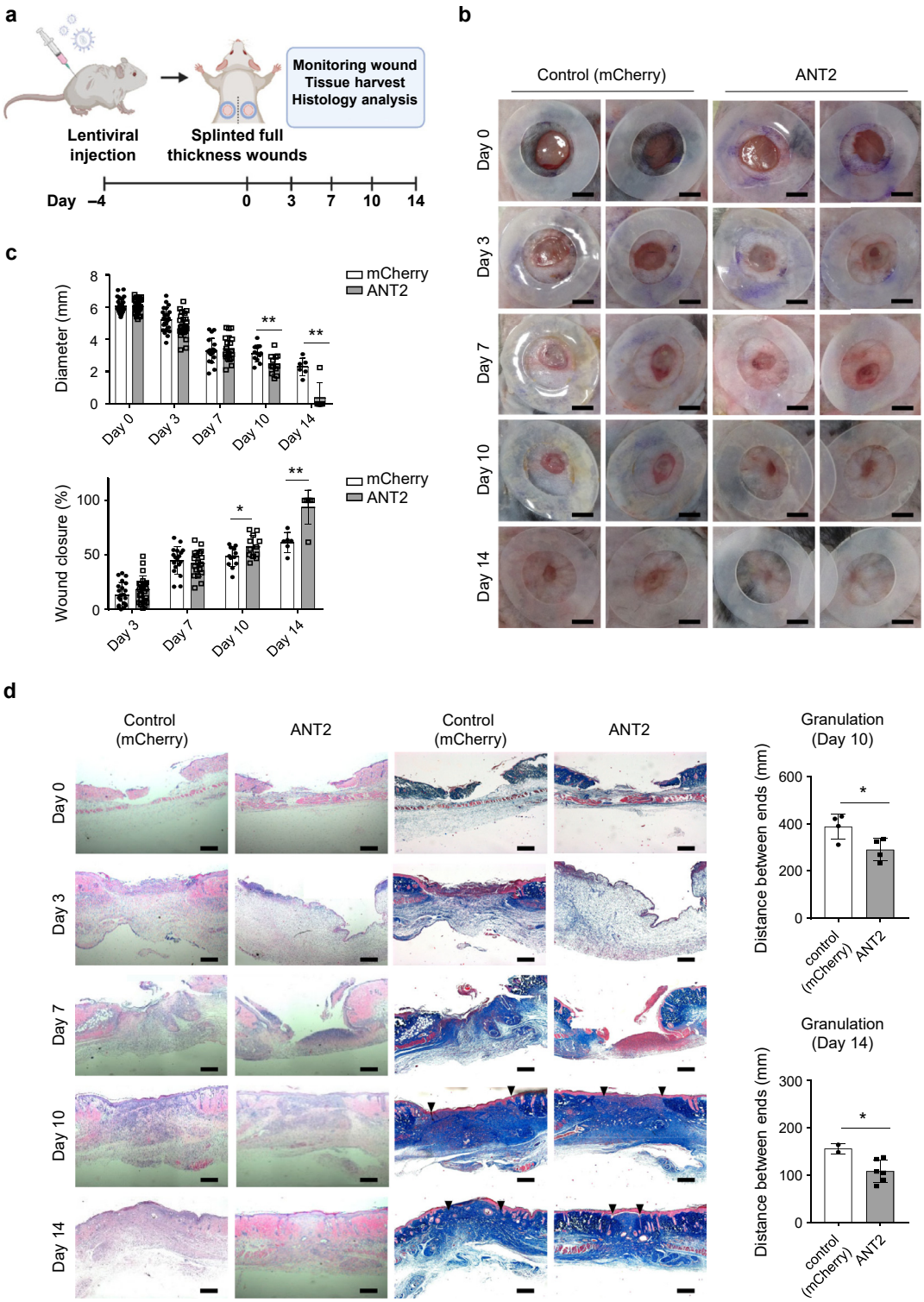

Figure 2. ANT2-induced accelerated wound healing in aged skin. (**a**) Experimental procedures for in vivo wound healing measurement. (**b, c**) Monitoring of time-dependent wound closure. Bar = 5 mm. Wound closure was quantified and presented as diameter, and wound closure was presented as percentage (%). The data are shown as the mean ± SD; n = 6–15 wound sites per group. (**d**) Microscopy images of H&E- and Masson trichrome–stained tissue specimens. Arrows mark the ends of the granulation tissue. Bar = 400 μm. The distance was quantified on the basis of the images. Each point represents a single wound. The data are shown as the mean ± SD; n = 2–6 wound sites per group. (**e–g**) IHC staining for (**e**) F4/80 (macrophages) and Ly6G (neutrophils) in the wound site on day 3 and for (**f, g**) Ki-67 (proliferation) and Cd31 (angiogenesis) on days 7 and 14. All fluorescence images below show the validation of mCherry (control) or ANT2 overexpression in the corresponding tissue. Slides were counterstained with hematoxylin (IHC-stained slides) or DAPI (fluorescent slides). Bar = 200 μm (lower magnification) or 10 μm (higher magnification). The number of brown spots was quantified with IHC tools in ImageJ software. The data are shown as the mean ± SD. Each point represents the number of counted (positively stained) cells per view field. For statistical analyses in **c–g**, $^{*}P \leq 0.05$, $^{**}P \leq 0.01$, $^{***}P \leq 0.001$, and $^{****}P \leq 0.0001$ as determined by multiple *t*-tests (for **c**) or unpaired *t*-test (for **d–g**). IHC, immunohistochemical.

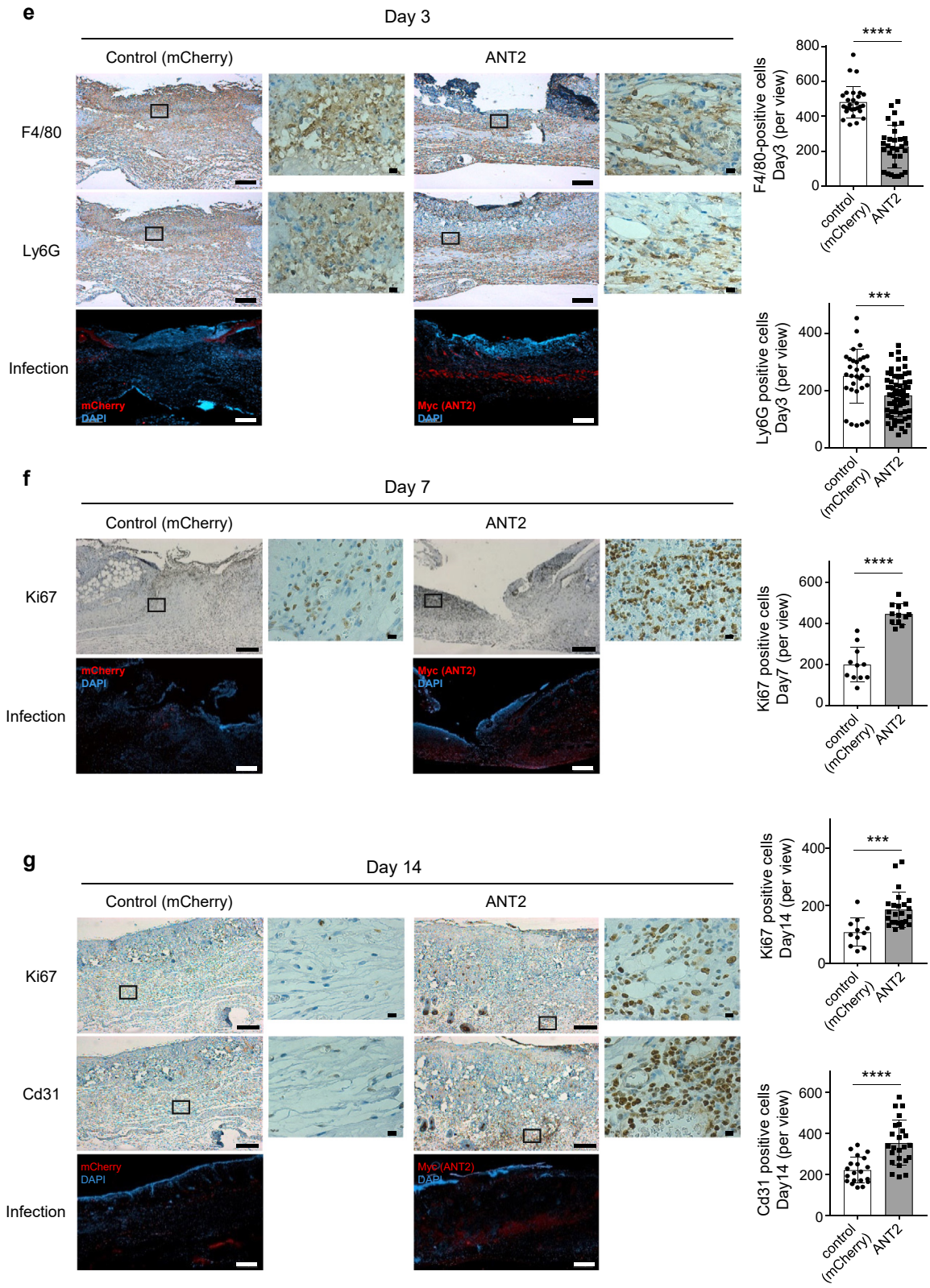

Figure 2. Continued.

mitochondria, similar to that observed in senescent HDFs. Notably, no significant difference was found in the amount of mitochondrial superoxide, mitochondrial membrane potential, or opening of the mitochondrial transition pore between the LacZ-overexpressing (control) and ANT2-OE cells (Supplementary Figure S7a). Furthermore, we examined the ultrastructure of mitochondria in aged mouse skin. We observed a loss of cristae and altered mitochondria morphology in the old group and mCherry (control) group. On the other hand, intact mitochondria were observed in the ANT2 group,

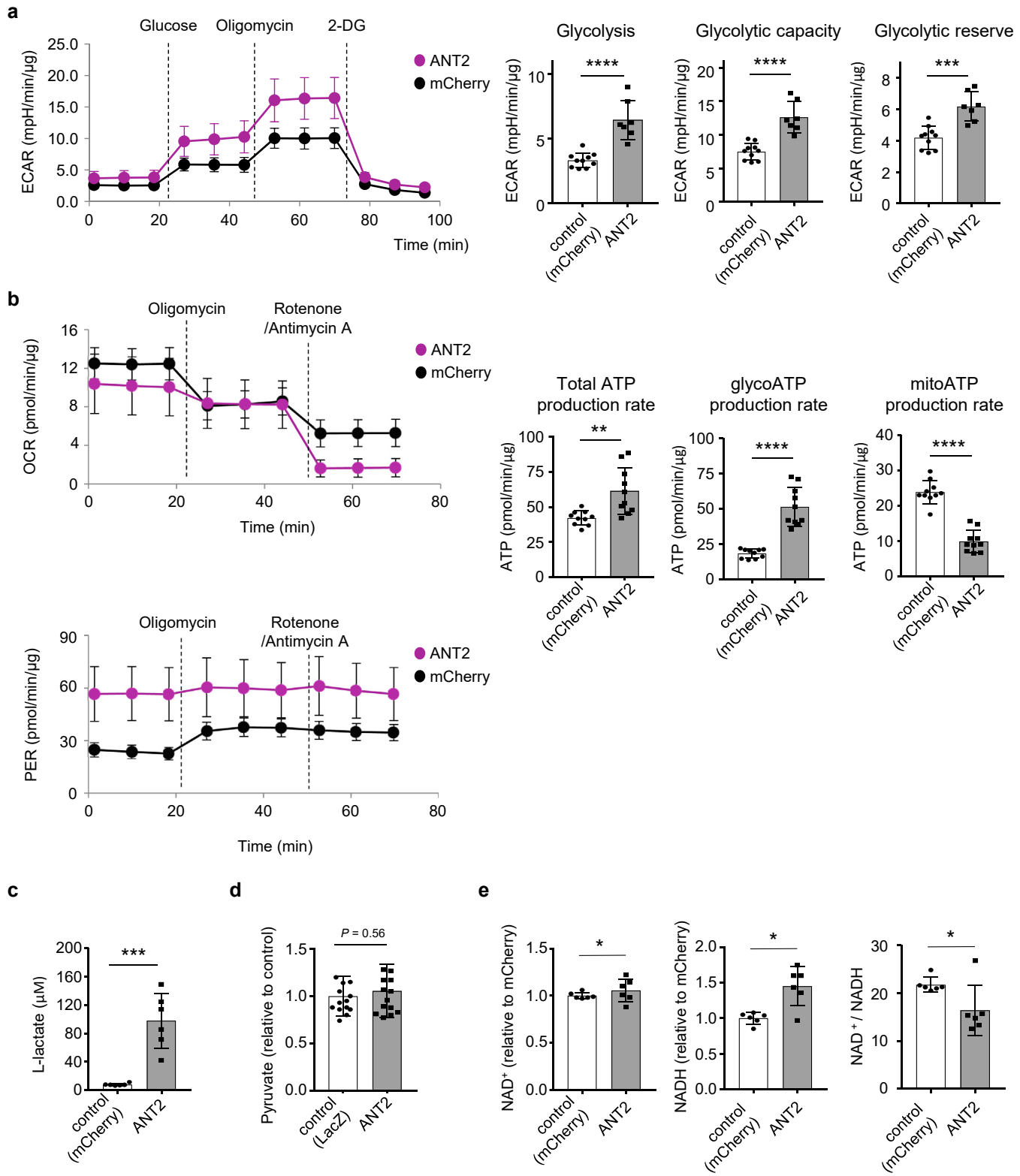

Figure 3. ANT2-mediated mitochondrial energy metabolism shift to glycolysis in senescent HDFs. (**a**) Glycolysis stress test while monitoring ECAR in mCherry-OE (control) and ANT2-OE senescent HDFs. Basal glycolysis, glycolytic capacity, and glycolytic reserve were quantified. The data are shown as the mean ± SD; n = 7–10 samples per experiment. (**b**) Real-time ATP rate assay based on the OCR and PER in mCherry-OE (control) and ANT2-OE senescent HDFs. The total ATP production rate, glycolytic ATP production rate, and mitochondrial ATP production rate were quantified. The data are shown as the mean ± SD; n = 10 samples per experiment. The black dotted lines indicate when the corresponding chemicals were added to the cells. (**c**–**e**) Significant differences in lactate, pyruvate, NAD^+, NADH, and NAD^+/NADH ratio between mCherry-OE (control) and ANT2-OE senescent HDFs. The data are shown as the mean ± SD; n = 6–13 samples per experiment. For statistical analyses in **a**–**e**, $*P \leq 0.05$ and $**P \leq 0.01$ as determined by unpaired *t*-test. 2-DG, 2-deoxy-D-glucose; ANT2-OE, ANT2-overexpressing; ATP, adenosine triphosphate; ECAR, extracellular acidification rate; HDF, human dermal fibroblast; mCherry-OE, mCherry-overexpressing; min, minute; OCR, oxygen consumption rate; PER, proton efflux rate.

similar to that observed in the young group (Figure 4d). The aging- or ANT2-dependent changes in the ultrastructure in mitochondria were similar to those observed in HDFs (Supplementary Figure S7b).

Mitochondrial fragmentation and fission promote the clearance of irreversibly damaged mitochondria by mitophagy (Fu et al., 2020). In aging, the mitophagy rate declines, resulting in the gradual accumulation of mitochondria, which leads to decreased cellular function (Detienne et al., 2016). Interestingly, in transmission electron microscopy images, the structure of organelles surrounding mitochondria was observed in the ANT2-OE group of aged mouse skin as well as in senescent HDFs (Figure 4d and Supplementary Figure S7b). In addition, the ANT2-OE group cells showed a narrower endoplasmic reticulum structure, similar to that of young HDFs, compared with the extended endoplasmic reticulum characteristic of the aging phenotype (Rellmann and Dreier, 2018; Truschel et al., 2018) observed in the mCherry-OE cells (control) and old HDFs (Supplementary Figure S7b). To determine whether ANT2 induces mitophagy, we measured the expression levels of mitophagy markers. The ANT2-OE cells exhibited increased expression of Parkin and PINK1 and decreased p62 expression (Figure 4e) compared with the mCherry-OE (control) cells. Similarly, Parkin was upregulated in the ANT2-OE aged mouse skin (Supplementary Figure S7c). According to previous reports, adenine nucleotide translocase leads to mitophagy independent of nucleotide exchange (Hoshino et al., 2019), which supports our observations. Taken together, these results indicate that ANT2 overexpression induces mitophagy to remove dysfunctional mitochondria in aging cells.

To elucidate the role of mitophagy induction on the wound healing–related phenotypes of ANT2-OE senescent HDFs, we evaluated cell proliferation (by measuring 5-ethynyl-20-deoxyuridine incorporation) and cell migration (by measuring scratch wound healing) in the presence of mdivi-1 as a mitophagy inhibitor or oligomycin as an oxidative phosphorylation inhibitor. Interestingly, mdivi-1 nullified the ANT2-induced acceleration of cell migration and 5-ethynyl-20-deoxyuridine incorporation (Supplementary Figure S8a and b). Meanwhile, oligomycin did not show a significant effect on the phenotypes (Supplementary Figure S8a and b). These data collectively suggest that mitophagy activation in ANT2-OE cells contributes to cellular remodeling to improve wound healing in aged tissues.

ANT2 overexpression downregulates proinflammatory cytokine release and senescence-associated secretary phenotype expression in aging

To explore the key regulator of ANT2-mediated wound healing effects in aging, we performed RNA-seq–based gene expression profiling in mCherry-OE (control) and ANT2-OE senescent HDFs (Figure 5a). Enrichment analysis of the Gene Ontology biological process category indicated that genes involved in the cellular response to cytokine-related processes, including cytokine production, inflammatory response, and chemokine production, were significantly enriched (Figure 5b). In addition, genes involved in cell proliferation, cell migration, extracellular structure organization, angiogenesis, regulation of wound healing, protein refolding, and cellular response to unfolded protein, which are closely related to the wound healing process, were also significantly enriched in the Gene Ontology biological process terms. The results of gene set enrichment analysis (Subramanian et al., 2005) showed that gene sets in cytokine production and cellular senescence were negatively correlated with ANT2 overexpression, whereas heat shock protein binding, extracellular matrix structural constituent, positive regulation of fibroblast migration, and positive regulation of G1/S transition of mitotic cell cycle were positively correlated with ANT2 overexpression (Figure 5c).

To verify the RNA-seq results, we measured the expression levels of inflammatory cytokines in the mCherry-OE (control) and ANT2-OE cells. As a result of RT-qPCR, the expression of the proinflammatory cytokine or senescence-associated secretory phenotype genes, including *CXCL1*, *CXCL2*, *CCL5*, *IL6*, *IL15*, *TNFα*, *IL1A*, *CXCL8*, and *IGFBP3*, was decreased in the ANT2-OE senescent HDFs (Figure 5d). Similar results were also found through ELISAs performed using the postwound skin obtained from aged mice, which showed reduced secretion of TNFα on day 10 in the ANT2 group, and by RT-qPCR, which showed decreased expression of the proinflammatory cytokine genes, including *Cxcl5*, *Il1α*, *Cxcl15*, and *Igfbp3* in the ANT2 group compared with those in the mCherry (control) group on day 3 (Figure 5e and Supplementary Figure S9a). In addition, the expression levels of the wound healing–related genes, including those related to angiogenesis (e.g., *TIMP1* and *LAMA2*) and extracellular matrix (e.g., *COL1A1* and *COLA2*), were upregulated (Figure 5d), which was associated with an increase in CD31-positive cells and facilitated the healing of aged mouse skin in the ANT2 group.

Notably, among the HSP70 family members, HSPA6 expression was markedly increased in the ANT2-OE cells, according to RNA-seq data, which was confirmed by RT-qPCR and western blot analysis (Figure 5d and f). Consistently, HSP70 expression was significantly increased in the mouse skin of the ANT2 group (Supplementary Figure S9b). In previous studies, HSP70 was considered a wound-healing agent because it inhibited proinflammatory cytokine levels and ameliorated cellular senescence (Jacquier-Sarlin et al., 1994; Ko et al., 2021). To determine whether the decreased expression of proinflammatory cytokine genes in the ANT2-OE cells was due to the increased expression of HSPA6, we knocked down HSPA6 expression in the mCherry-OE (control) or ANT2-OE cells using short interfering RNA against HSPA6 (Supplementary Figure S10a) and compared the expression of proinflammatory cytokine genes. Interestingly, the expression of many inflammatory cytokine genes, including *CXCL1*, *IL6*, *IL15*, and *IL1A*, was increased in the ANT2-OE cells after short interfering RNA treatment (Figure 5g). Similarly, VER-155008, an HSP70 inhibitor, also induced the expression of the inflammatory cytokine genes, including *IL6*, *IL15*, *LIF*, and *IL1A*, in the ANT2-OE cells (Supplementary Figure S10b). Collectively, our data show that ANT2 specifically increases the expression of HSPA6 in the HSP70 family, which reduces the expression of senescence-associated secretory phenotype and proinflammatory cytokines in aging. As an extended study to elucidate the molecular mechanism of the anti-inflammatory effect of ANT2 in aging, we investigated whether the change in energy metabolism toward glycolysis by ANT2 overexpression, as shown in Figure 3, affected the expression of

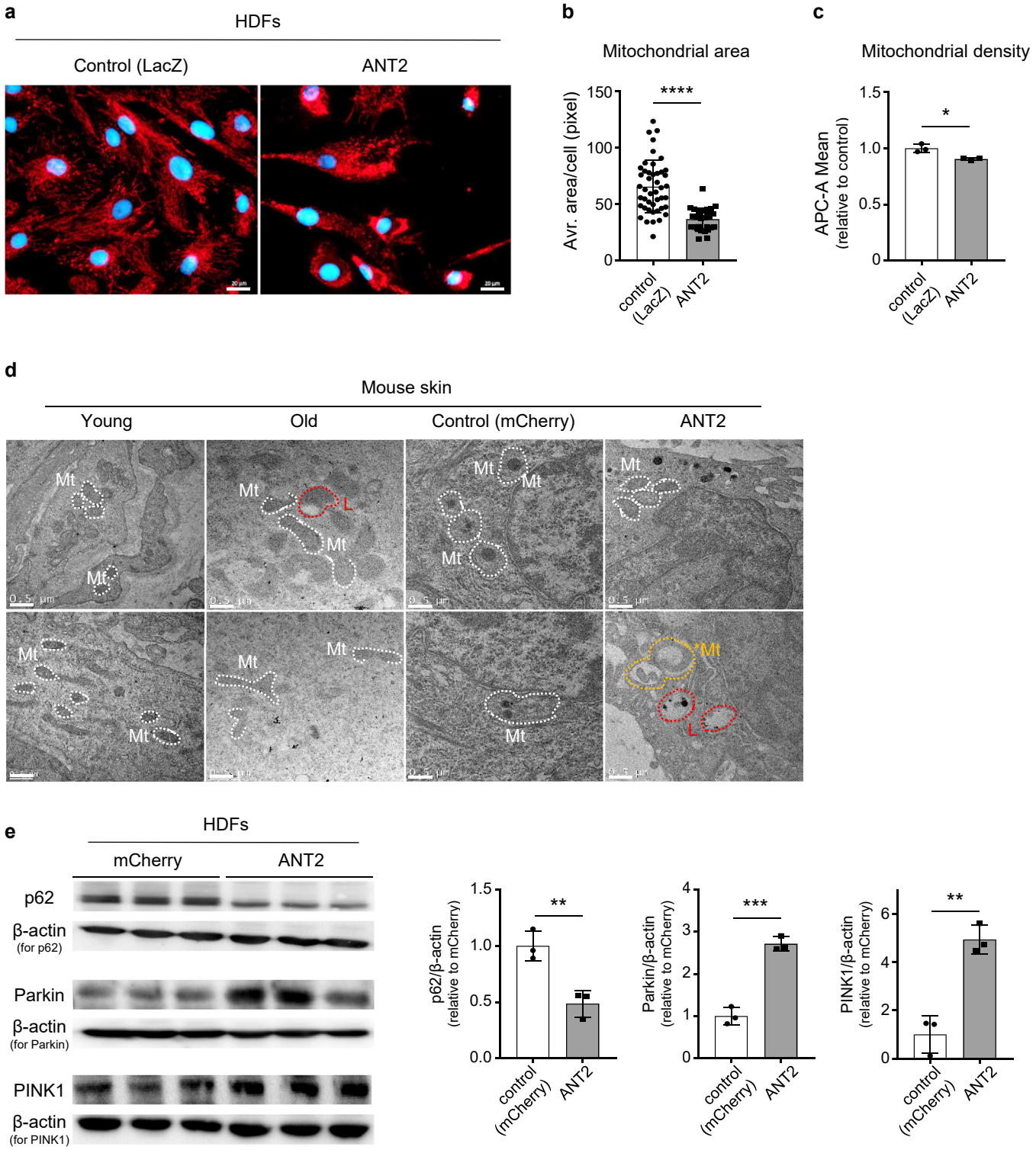

Figure 4. ANT2 induced mitophagy in aging. (**a**) Intracellular mitochondrial morphology in LacZ-OE (control) and ANT2-OE senescent HDFs. Bar = 20 μm. (**b**) Quantification of the mitochondrial area per cell. The data are shown as the mean ± SD; n > 25 cells per group. (**c**) Mitochondrial density as indicated by MitoTracker deep red and flow cytometry. The data are shown as the mean ± SD; n (biological replicate) = 3. (**d**) TEM images of mitochondria in mouse skin. Mt denotes mitochondria, *Mt denotes mitophagy, and L denotes lysosome. Bar = 0.5 μm. (**e**) Immunoblots and quantification of p62, Parkin, and PINK1 expression in mCherry-OE (control) and ANT2-OE senescent HDFs. β-Actin was used for normalization. The data are shown as the mean ± SD; n (biological replicate) = 3. For statistical analyses in **b, c,** and **e**, $*P \leq 0.05$, $**P \leq 0.01$, $***P \leq 0.001$, and $****P \leq 0.0001$ as determined by unpaired *t*-test. ANT2-OE, ANT2-overexpressing; HDF, human dermal fibroblast; LacZ-OE, LacZ-overexpressing; mCherry-OE, mCherry-overexpressing; TEM, transmission electron microscopy.

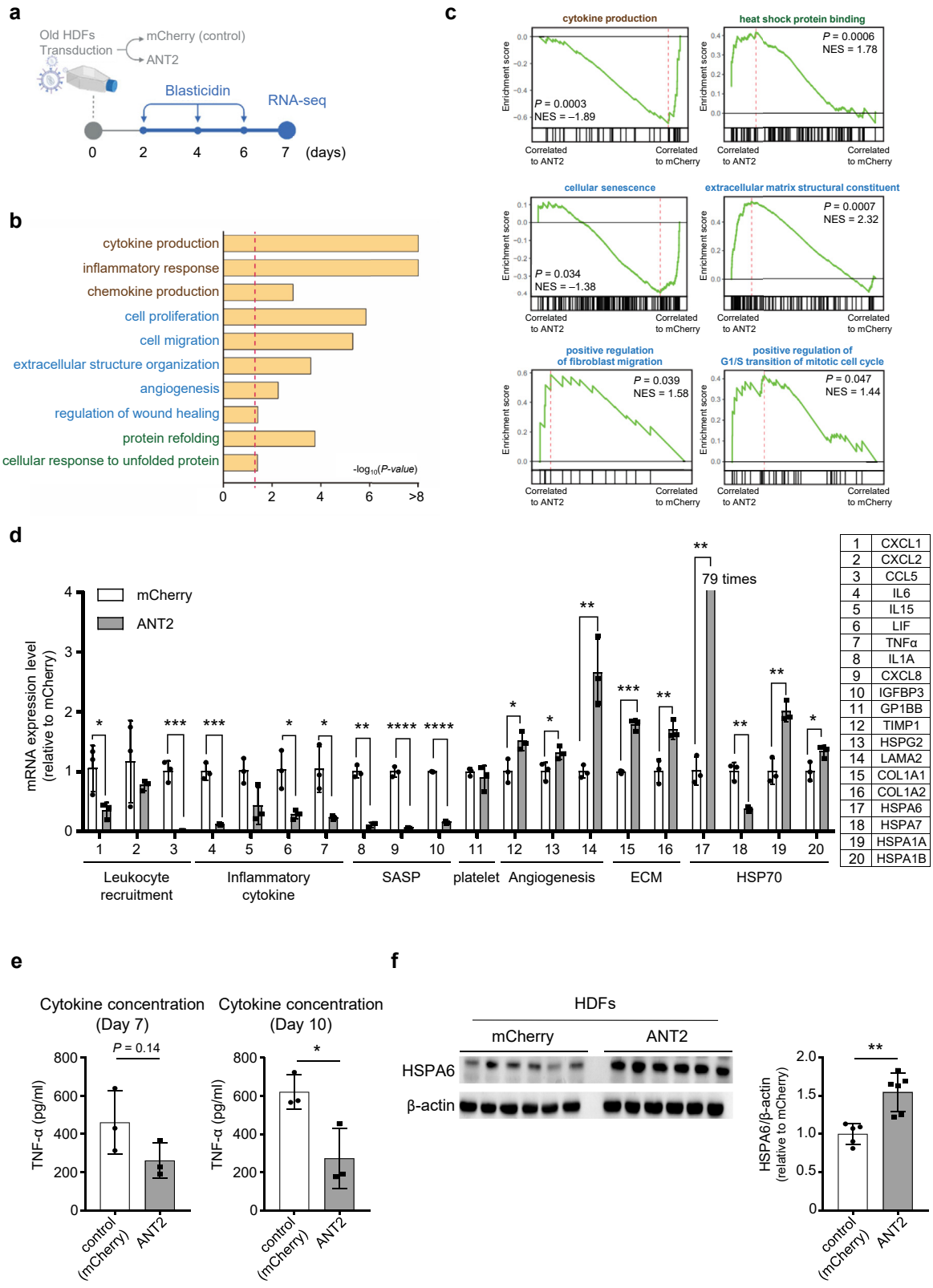

Figure 5. The ANT2−HSPA6 axis downregulates proinflammatory cytokine expression during wound healing in aging. (**a**) Experimental process for RNA-seq–based gene expression profiling in mCherry-OE (control) and ANT2-OE cells. (**b**) GO enriched terms in the RNA-seq dataset. (**c**) GSEA plots showing the differentially expressed genes identified between the mCherry-OE and ANT2-OE cells. (**d**) The RNA-seq results obtained with mCherry-OE (control) and ANT2-OE senescent HDFs were verified with RT−qPCR. The data are shown as the mean ± SD; n (biological replicate) = 3. (**e**) Expression of the proinflammatory cytokine TNF-α as measured by ELISA on days 7 and 10. (**f**) Immunoblots and quantification of HSPA6 expression in mCherry-OE (control) and ANT2-OE senescent HDFs. The data are shown as the mean ± SD; n (biological replicate) = 6. β-Actin was used for normalization. (**g**) The expression of proinflammatory cytokine genes measured by RT−qPCR after HSPA6 expression was knocked down using siRNA in mCherry-OE (control) and ANT2-OE senescent HDFs. The data are shown as the mean ± SD; n (biological replicate) = 3. (**h**) Schematic models showing ANT2 involvement in facilitating wound

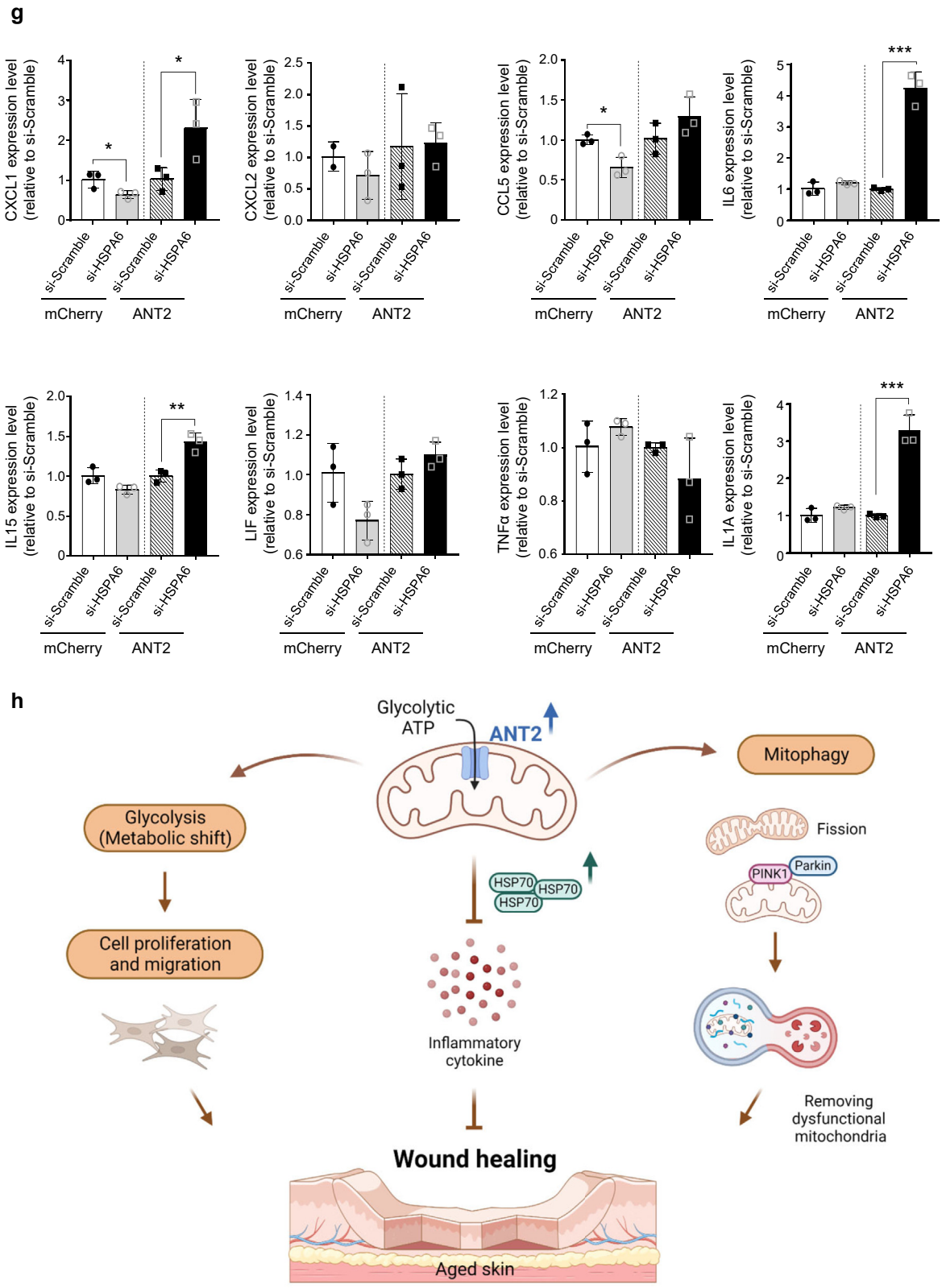

Figure 5. Continued.

healing in aged skin. The arrows and suppression symbols indicate activation and inhibition reactions, respectively. For statistical analyses in **b**−**g**, $*P \leq 0.05$, $**P \leq 0.01$, $***P \leq 0.001$, and $****P \leq 0.0001$ as determined by unpaired *t*-test. si denotes small interfering RNA. ANT2-OE, ANT2-overexpressing; ECM, extracellular matrix; GO, Gene Ontology; GSEA, gene set enrichment analysis; HDF, human dermal fibroblast; mCherry-OE, mCherry-overexpressing; NES, normalized enrichment score; RNA-seq, RNA-sequencing; SASP, senescence-associated secretory phenotype; siRNA, short interfering RNA.

inflammatory cytokines. When glycolysis was blocked by treatment with 20 mM sodium oxamate or a low-glucose medium for 48 hours, the expression levels of the proinflammatory cytokine genes, including *CXCL1*, *CXCL8*, *IL1A*, *IL6*, and *TNFα*, were significantly upregulated in the ANT2-OE senescent HDFs (Supplementary Figure S11a and b). Consistent with the reverse correlation between the glycolysis activity and proinflammatory cytokine expression in this context, oligomycin treatment, which inhibits mitochondrial ATP production and consequently activates glycolysis, exhibited further attenuation of several proinflammatory cytokines, including *CXCL1*, *IL6*, and *IL1A* in the ANT2-OE senescent HDFs (Supplementary Figure S11c). Meanwhile, mdivi-1 did not modulate the expression of these cytokines (Supplementary Figure S11d). It was previously reported that the overexpression of HSP70 led to a shift in energy metabolism through increased glycolytic metabolism (Wang et al., 2012), which implies that there might be crosstalk between glycolysis and the HSP70-mediated proinflammatory cytokine expression in ANT2 overexpression conditions. Taken together, our data collectively suggest that ANT2-dependent HSPA6 upregulation and enhanced glycolytic capacity attenuate unnecessary inflammatory signaling, contributing to wound healing.

DISCUSSION

Wound healing is primarily influenced by fine-tuned cellular functions to maintain tissue homeostasis, for which the supply of sufficient energy is essential (Kotwal and Chien, 2017; Wall et al., 2008; Wang et al., 2009). Continuous ATP synthesis is required to maintain these energy levels, and ATP is consumed in every aspect of the wound healing process as well as to fuel cellular functions such as protein and lipid biosynthesis, signal transduction, cell mitosis and migration, and GF production (Clémençon et al., 2013). Because energy homeostasis is vital, a better understanding of the influence of this mechanism on wound healing is needed. ANT2, which imports cytosolic ATP into the mitochondrial matrix, is closely associated with mitochondrial integrity (Fan et al., 2020). Considering the reduced levels of ANT2 in aged mouse and senescent cells (Hubackova et al., 2019b; Kim et al., 2012), which was consistent with our observation, it is reasonable to speculate that ANT2 may play a role in restoring energy homeostasis by supplying sufficient ATP to the matrix and enhancing cellular function in aging. Our results collectively suggest that ANT2 appears to be a potential candidate to enhance wound healing by activating glycolysis-dependent ATP generation and enhancing the function of organelles, cells, and tissues in aging.

Cellular senescence is a conserved mechanism that occurs during aging (Kirkland and Tchkonia, 2017). Senescent fibroblasts accumulate in aged skin and result in chronic nonhealing wounds (Chapman et al., 2019, Samdavid Thanapaul et al., 2022). For example, senescent cells secrete a series of senescence-associated secretory phenotype molecules that modulate the surrounding microenvironment, directly or indirectly affecting various processes during regeneration, including angiogenesis. Preventing cellular senescence or eliminating senescent cells mitigates chronic wounds (Wang and Shi, 2020). Therefore, targeting senescent cells may be a therapeutic strategy to ameliorate impaired wound healing in aged skin (Ding et al., 2021). Our data showed that the induction of ANT2 alleviated several key features of cellular senescence, resulting in increased cell proliferation and migration as well as reduced lipofuscin levels. Aged skin and senescent dermal cells commonly show low efficiency of ATP synthesis because of the accumulation of dysfunctional mitochondria (Chapman et al., 2019). Interestingly, ANT2 is associated with the maintenance of mitochondrial potential and integrity during glycolysis, when the electron transport chain function is impaired or its contribution to ATP generation is minor (Giraud et al., 1998; Hubackova et al., 2019b; Pedersen, 1978). We found that the ANT2 enhanced the glycolytic capacity and total ATP production. We also observed that an increase in the ANT2−mediated glycolytic capacity enhanced the migratory ability and reduced the expression of the inflammatory cytokines in senescent cells. These outcomes were consistent with the characteristics of glucose metabolism, which exerts a protective effect on the skin by increasing cell proliferation factors and inhibiting proinflammatory cytokines (Yoo et al., 2015). Although there is the limitation that hallmarks of in vitro fibroblast senescence do not completely correspond with those of human fibroblasts isolated from intrinsically aged skin (Waldera Lupa et al., 2015), our findings imply that the recovery of ANT2 levels triggers the alleviation of cellular senescence, resulting in stimulation of the wound repair process of aging.

Mitochondrial morphology is closely related to mitophagy, which gradually replaces damaged, enlarged, and dysfunctional mitochondria with normal organelles (Mishra and Chan, 2016). Senescent cells present a mass of enlarged mitochondria owing to their inadequate mitophagy capacity, which is caused by impaired mitochondrial fission and inactive lysosomes (Brunk and Terman, 2002). Notably, adenine nucleotide translocase plays a critical role in mitophagy by interacting with TIM23 and subsequently stabilizing PINK1 (Hoshino et al., 2019). Moreover, ANT2 overexpression restored the altered mitochondrial morphology in senescent cells exposed to mitochondria-targeted tamoxifen (Hubackova et al., 2019a). We also confirmed that ANT2 activated PINK1/Parkin-mediated mitophagy in cellular senescence. Notably, HSP70, which is significantly upregulated by ANT2 overexpression in our study, is known to participate in PINK1-mediated mitophagy by regulating the stability of PINK1 (Zheng et al., 2018). In addition, caspase activation shown in ANT2-OE senescent HDFs has been reported to be associated with macroautophagy regulation (An et al., 2020; Jeong et al., 2011). Taken together, these data indicate that ANT2 is important to remove damaged mitochondria while maintaining energy homeostasis in aging. This mitochondrial change could be a reason for reduced maximal respiration in the ANT2-OE senescent cells.

Furthermore, it is noteworthy that ANT2 markedly induced HSPA6 expression in senescent HDFs. HSPA6 is a member of the HSP70 family, known to be a key accelerator of wound healing by activating the immune system and promoting fibroblast proliferation (Jiang et al., 2016; Kovalchin et al., 2006). We found that ANT2 decreased the expression of proinflammatory cytokines in senescent HDFs, which prompted us to speculate that the ANT2−HSP70 axis might be linked to inflammation. We showed that knocking down the expression of HSPA6 by short interfering RNA or an

HSP70 inhibitor in ANT2-OE cells reactivated the expression of proinflammatory cytokines. Proinflammatory cytokines in fibroblasts are stressors that exacerbate the chronic wound state and cellular senescence (Harding et al., 2005). Thus, downregulating the expression of proinflammatory cytokines enhanced the healing ability to overcome the inflammatory phase of a chronic wound state (Maxson et al., 2012). Moreover, histological analysis revealed that ANT2 accelerated wound healing by resolving inflammatory delay and promoting proliferation in aging. However, the lack of an HSPA6 ortholog in mice and rats limited our work (Maxson et al., 2012). Other molecular mechanisms, including the metabolic reprogramming toward glycolysis mentioned earlier, could be presumed as part of the ANT2-dependent downregulation of proinflammatory cytokines. Notably, HSP70 plays a role in shifting energy metabolism toward glycolysis (Wang et al., 2012). These findings and previous evidence are expected to promote further investigation into the relationship between ANT2 and HSP70 in the recovery of cellular senescence and acceleration of wound healing.

The system we studied was the acute wound healing in aged skin, in which senescent cells are accumulated, and tissue homeostasis is disturbed (Franco et al., 2022; Sindrilaru et al., 2011). In acute wound healing, it has been reported that PDGF-AA from cells displaying senescent phenotypes in a spatiotemporal manner plays a beneficial role in the repair process (Demaria et al., 2014). Meanwhile, one of the characteristics of senescent cells in physiological aging is the secretion of proinflammatory cytokines, which is a contributor to the chronic inflammation associated with delayed wound healing (Freund et al., 2010). In this study, we revealed that ANT2 overexpression modulated the degree of inflammation in the aged mouse skin and confirmed that ANT2 overexpression downregulated the gene expression related to proinflammatory cytokines in senescent HDFs. In further studies, it is necessary (i) to differentiate the cell types between senescent cells accumulated in aged tissues and cells having senescent phenotypes involving tissue remodeling and (ii) to evaluate the age-dependent appearance of temporarily emerging senescent cells during wound repair.

In conclusion, we identified the function of ANT2 to promote wound healing in aged skin. Our data revealed the specific roles of ANT2 in aging: ANT2 influences the overall wound healing by promoting a metabolic shift to increase total ATP production in a glycolysis-dependent manner, inducing cell proliferation and mitophagy, and modulating inflammatory cytokine production (Figure 5h). Importantly, these findings bridge two processes that show functional decline with aging, namely regeneration and energy metabolism. Our findings illuminate a potential therapeutic approach on the basis of a mitochondrial ATP translocator for wound healing as well as senescence control in aged skin.

MATERIALS AND METHODS

Wound healing assay

C57BL/6 male mice (aged 25 months) were used for a wound healing assay following the ethics guidelines of the Laboratory Animal Research Center at the Daegu Gyeongbuk Institute of Science and Technology (Daegu, Republic of Korea) (approval number DGIST-IACUC-21090802-0000). A stented skin wound model was used to estimate the kinetics of tissue repair (Choi et al., 2016; Dunn et al., 2013; Finley et al., 2013). Specifically, mice were anesthetized using 1.5% isoflurane in oxygen (flow rate = 1 l/min, Isotroy 100, Troikaa Pharmaceutical, Ahmedabad, India), and anesthesia was maintained in 1% isoflurane (SomnoSuite Anesthesia System, Kent Scientific, Tokyo, Japan). The surgical region on the dorsal skin was prepared by removing fur with clippers and applying depilatory cream, followed by cleansing with three alternating scrubs (sterilized water, alcohol, and povidone-iodine). Subcutaneous lentiviral particle injection (100 μl per site with approximately 0.6×10^6 particles/μl) was administered directly to the surgical region, and the region was marked and covered. Four days after injection, full-thickness excisional wounds were created using a sterile 6-mm biopsy punch (Kai Medical, Seki City, Japan) on either side of the midline of the mouse. In the regions surrounding the wounds, 0.5-mm ring-shaped silicone splints (1.0 and 1.5 mm outer and inner diameter, respectively) were affixed with tissue adhesive (VetBond 1469c, 3M, Saint Paul, MN). A transparent occlusive dressing (Tegaderm Film 1622 W, 3M) was placed over the wounds to stabilize them. After surgery, the mice were housed in individual cages under a warming lamp. The wound area was measured, and samples were excised at different time points (days 0, 3, 7, 10, and 14) for histological and gene expression analyses.

Cell culture

HDFs obtained from neonatal foreskin were purchased from ATCC (PCS-201-010, ATCC, Manassas, VA) and maintained in DMEM (LM001-05, WELGENE, Gyeongsan, Korea) supplemented with 10% fetal bovine serum (S001-01, WELGENE), 1% penicillin (100 units/ml), 10 μg/ml streptomycin, and 25 ng/ml amphotericin B (LS203-01, WELGENE). The cells were maintained at 37 °C in 5% carbon dioxide and routinely split at ratios of 1:4 during early passages (up to passage 45), 1:3 (passages 46−47), and 1:2 during late passages (passages 48−50). Determination of HDF senescence was based on the following criteria: >90% of the cells were stained with senescence-associated β-galactosidase assay (number 9860, Cell Signaling Technology, Danvers, MA), and the population doubling time of the cell cultures was 14 days or more.

Cell migration assay

Lentiviral-mediated mCherry-OE (as a control) or ANT2-OE senescent HDFs (mCherry-OE or ANT2-OE, respectively) were seeded in 12-well plates. Once the cells reached 90% confluence, the monolayers were scratched with a 200-μl pipette tip. The plates were then incubated at 37 °C with 5% carbon dioxide for 62 hours. Images were acquired every 12 hours. For inhibition of glycolysis, the cells were treated with 20 mM sodium oxamate (sc-215880, ChemCruz, Santa Cruz Biotechnology, Dallas, TX), 20 mM 2-deoxy-D-glucose (D8357, Sigma-Aldrich, St. Louis, MO), or low-glucose DMEM (LM 001-11, WELGENE) for 48 hours before cell monolayer scratching. For inhibition of HSP70, 10 μM VER-155008 (SML0271-5MG, Sigma-Aldrich) was added to the cell cultures. The same inhibitor concentrations were also used in a RT-qPCR assay.

Cellular metabolic flux measurement

ANT2-OE and mCherry-OE (control) cells were cultured in Seahorse XFe24 cell culture plates (V7-PS 100777-004, Seahorse Biosciences, Billerica, MA) at a density of 2×10^4 cells/well 1 day before analysis. On the day of the analysis, the media were replaced with fresh media, and extracellular flux assay kits (Agilent Technologies, Palo Alto, CA) were equilibrated with XF calibrant (pH 7.4) (number 100840-000, Agilent Technologies). After incubation in a non−carbon dioxide

condition at 37 °C, the oxygen consumption rate and ECAR were simultaneously measured with a Seahorse XF metabolic analyzer (Agilent Technologies).

Mitochondrial respiration was analyzed with a Seahorse XF Cell Mito Stress Test Kit (number 103015-100, Agilent Technologies) according to the manufacturer's instructions. Specifically, Seahorse XF base medium (number 102353-100, Agilent Technologies) supplemented with 4,500 mg/l D-glucose, 1 μM sodium pyruvate, and 4 mM L-glutamine was used for the assay. The oxygen consumption rate was recorded after sequential injection of oligomycin (1 μM), carbonyl cyanide 4-(trifluoromethoxy)-phenylhydrazone (2 μM), and rotenone (0.5 μM). Glycolytic flux was measured with a Seahorse XF Glycolysis Stress Test Kit (number 103020-100, Agilent Technologies). For this assay, the ECAR was monitored in cells grown in pH-adjusted (at 7.4) Seahorse XF base medium supplemented with 2 mM L-glutamine and sequential injection of glucose (10 mM), oligomycin (1 μM), and 2-deoxy-D-glucose (50 mM). The ATP production rate was estimated by monitoring the oxygen consumption rate and ECAR after sequential injection of oligomycin (1.5 μM) and rotenone (0.5 μM) into the XF base medium (pH 7.4) supplemented with 10 mM D-glucose, 1 mM sodium pyruvate, and 2 mM L-glutamine. The raw data were normalized to the total cellular protein concentration in each well and analyzed with an XF Report Generator (Agilent Technologies).

Transmission electron microscopy

ANT2-OE or mCherry-OE senescent HDFs and proliferating HDF (young cell) pellets were obtained and fixed in 2.5% glutaraldehyde (in 0.1 M sodium cacodylate buffer) for 1 hour at room temperature. After washing with cacodylate buffer, the pellets were embedded in low-melting-point agarose (number 4250-050-02, Trevigen, Gaithersburg, MD) and cut into small pieces. Skin tissue samples from old mice infected with lentivirus for overexpressing mCherry or ANT2 and those from young mice were fixed in 2.5% glutaraldehyde and washed with 0.1 M cacodylate buffer. The fixed samples were incubated in 1% osmium tetroxide overnight at 4 °C. After washing with cacodylate buffer, the samples were dehydrated with a series of graded ethanol and 100% propylene oxide. The samples were then embedded in medium-intensity resin (nadic methyl anhydride, EPON epoxy, dodecenyl succinic anhydride, and benzyldimethylamine, Electron Microscopy Sciences, Hatfield, PA). Ultrathin sections were prepared using a cryo-ultramicrotome (EM UC7, Leica, Wetzlar, Germany) and stained with lead citrate and uranyl acetate. The sections were then imaged with a Bio- transmission electron microscope (FEI Tecnai G2 F20 TWIN TMP, Amsterdam, Netherlands).

Transcriptome analysis

After the completion of the wound healing assays, the mouse skin samples were immediately frozen at −80 °C. Total RNA was extracted from the frozen mouse skin samples or HDFs using QIAzol lysis reagent (number 79306, Qiagen, Hilden, Germany) on ice, following the manufacturer's instructions. RNA purity and concentration were determined with a NanoDrop One (Thermo Fisher Scientific, Waltham, MA) spectrophotometer. RNA integrity was assessed through electrophoresis. The samples were used for mRNA expression analysis.

The expression profiles of samples were compared using transcriptome sequencing data after sample quality control with a TapeStation RNA Screen Tape system and a next-generation sequencing library quality control with a TapeStation D1000 Screen Tape at Microgen (Seoul, Korea). Transcriptome expression profile differences between the ANT2-OE and mCherry-OE samples were determined on the basis of nbinomWaldTest using DESeq2. Transcripts with fold change ≥ 2 and Benjamini−Hochberg−adjusted P-values < 0.05 were considered to be differentially expressed mRNAs. Gene Ontology enrichment and Kyoto Encyclopedia of Genes and Genomes analyses were performed with all the differentially expressed mRNAs.

For the age-dependent ANT2 expression, public skin-aging RNA-seq data of human (Fleischer et al., 2018) and mouse (GSE75192 [Aramillo Irizar et al., 2018]) were analyzed. In the public human data, only fibroblast data with <10 passages were used for the data analysis to exclude the replicative-senescence effects from high-passaged samples. In the public mouse dataset, only skin data among various tissue data were selected and used for the data analysis. In this study, we reduced the group size to four by merging two age groups (ages 9 and 15 months) among five age groups on the basis of sample similarity. For RNA-seq processing, reads were aligned against the corresponding sample organism's reference genome (CRCh38 for human data and GRCm38.p6 for mouse data) using the STAR alignment tool (version 2.5.1a). To quantify the expression level of each gene, the binary alignment map files generated by the STAR (Dobin et al., 2013) were processed using the high-throughput sequence analysis software package (Anders et al., 2015). The DESeq2 R/Bioconductor package (Love et al., 2014) was used to perform differential expression analysis and statistical testing on the raw count data generated from the published dataset.

For the age-dependent ANT2 expression at the single-cell level, public single-cell RNA-seq data of human skin samples from four elderly (aged >60 years) and three young (aged <30 years) human females (Ahlers et al., 2022) were reanalyzed using Cell Ranger (version 3.0.2) and Seurat (version 2.3) software packages. The sequence data were aligned to the human reference genome (GRCh38) using Cell Ranger, and transcript quantification was performed using the count function in Cell Ranger. Cells with low gene expression (<200 genes) or high mitochondrial gene expression (>20%) were removed from further analysis. The expression matrix was then normalized using the LogNormalize and ScaleData methods, and the top 1,000 most variable genes were selected for principal component analysis. The first 30 principal components were used to identify cell clusters using the FindClusters function with a resolution of 1.0. The cell-type annotation was performed using the same markers as the previously reported (Ahlers et al., 2022). Specifically, we identified the cell markers for each cell type within the clusters and annotated each cluster accordingly.

Statistical analysis

All data were analyzed using GraphPad Prism, version 7 (GraphPad Software, San Diego, CA). Most of the analyses were performed using t-tests (and nonparametric tests). The wound healing analysis was performed with multiple t-tests (one per row as grouped analysis). The specific statistical analysis methods are described in the figure legends, and the results are presented. Statistical significance was set at $P < 0.05$.

For all other procedures, see Supplementary Materials and Methods.

Data availability statement

The RNA-sequencing dataset related to this article can be founded at https://www.ncbi.nlm.nih.gov/geo/query/acc.cgi?acc=GSE206141, hosted at the Gene Expression Omnibus database under accession identification GSE206141.

ORCIDs
Seung-Hwa Woo: http://orcid.org/0000-0002-9336-4457
Yun Jeong Mo: http://orcid.org/0009-0006-3319-1722

Yun-Il Lee: http://orcid.org/0000-0001-9203-2234
Ji Hwan Park: http://orcid.org/0000-0001-9098-3204
Daehee Hwang: http://orcid.org/0000-0002-7553-0044
Tae Jun Park: http://orcid.org/0000-0002-8862-1834
Hee Young Kang: http://orcid.org/0000-0001-8697-4292
Sang Chul Park: http://orcid.org/0000-0002-7930-0596
Young-Sam Lee: http://orcid.org/0000-0002-4702-0127

CONFLICT OF INTEREST

The authors state no conflict of interest.

ACKNOWLEDGMENTS

This study was supported by the Basic Research Program (NRF-2020R1A2C2013416, NRF-2020M3A9D8038014, and NRF-2022R1A4A2000703) through the National Research Foundation of Korea funded by the Ministry of Science, ICT and Technology. This research was also supported by Chonnam National University R&D Program Grant for Research Chair Professor. Thanks to Prof. Jaewon Lee (Pusan National University) who kindly gifted anti-ANT2 antibody. Schematic figures were adapted from scheme of wound healing test, scheme of RNA sequencing, and summary by BioRender.com (2022), retrieved from https://app.biorender.com/biorender-templates.

AUTHOR CONTRIBUTIONS

Conceptualization: YSL, SCP; Data Curation: SHW, YJM, TJP, HYK, JHP; Formal Analysis: JHP, DW; Supervision: YSL; Writing - Original Draft Preparation: SHW, YSL; Writing - Review and Editing: SHW, YIL, TJP, DH, SCP, YSL

SUPPLEMENTARY MATERIAL

Supplementary material is linked to the online version of the paper at www.jidonline.org, and at https://doi.org/10.1016/j.jid.2023.05.002.

REFERENCES

Ahlers JMD, Falckenhayn C, Holzscheck N, Solé-Boldo L, Schütz S, Wenck H, et al. Single-cell RNA profiling of human skin reveals age-related loss of dermal sheath cells and their contribution to a juvenile phenotype. Front Genet 2022;12:797747.

An HK, Chung KM, Park H, Hong J, Gim JE, Choi H, et al. CASP9 (caspase 9) is essential for autophagosome maturation through regulation of mitochondrial homeostasis. Autophagy 2020;16:1598–617.

Anders S, Pyl PT, Huber W. HTSeq–a Python framework to work with high-throughput sequencing data. Bioinformatics 2015;31:166–9.

Aramillo Irizar P, Schäuble S, Esser D, Groth M, Frahm C, Priebe S, et al. Transcriptomic alterations during ageing reflect the shift from cancer to degenerative diseases in the elderly [published correction appears in Nat Commun 2019;10:2459] Nat Commun 2018;9:327.

Bainbridge P. Wound healing and the role of fibroblasts. J Wound Care 2013;22(407–8):10–2.

Beckert S, Farrahi F, Aslam RS, Scheuenstuhl H, Königsrainer A, Hussain MZ, et al. Lactate stimulates endothelial cell migration. Wound Repair Regen 2006;14:321–4.

Bertolo A, Baur M, Guerrero J, Pötzel T, Stoyanov J. Autofluorescence is a reliable in vitro marker of cellular senescence in human mesenchymal stromal cells. Sci Rep 2019;9:2074.

Boehm M, Nabel EG. Cell cycle and cell migration: new pieces to the puzzle. Circulation 2001;103:2879–81.

Braiman-Wiksman L, Solomonik I, Spira R, Tennenbaum T. Novel insights into wound healing sequence of events. Toxicol Pathol 2007;35:767–79.

Brunk UT, Terman A. The mitochondrial-lysosomal axis theory of aging: accumulation of damaged mitochondria as a result of imperfect autophagocytosis. Eur J Biochem 2002;269:1996–2002.

Buckley CD, Pilling D, Lord JM, Akbar AN, Scheel-Toellner D, Salmon M. Fibroblasts regulate the switch from acute resolving to chronic persistent inflammation. Trends Immunol 2001;22:199–204.

Caputa G, Flachsmann LJ, Cameron AM. Macrophage metabolism: a wound-healing perspective. Immunol Cell Biol 2019;97:268–78.

Chapman J, Fielder E, Passos JF. Mitochondrial dysfunction and cell senescence: deciphering a complex relationship. FEBS Lett 2019;593:1566–79.

Chevrollier A, Loiseau D, Reynier P, Stepien G. Adenine nucleotide translocase 2 is a key mitochondrial protein in cancer metabolism. Biochim Biophys Acta 2011;1807:562–7.

Chistiakov DA, Sobenin IA, Revin VV, Orekhov AN, Bobryshev YV. Mitochondrial aging and age-related dysfunction of mitochondria. BioMed Res Int 2014;2014:238463.

Choi SK, Park JK, Kim JH, Lee KM, Kim E, Jeong KS, et al. Integrin-binding elastin-like polypeptide as an in situ gelling delivery matrix enhances the therapeutic efficacy of adipose stem cells in healing full-thickness cutaneous wounds. J Control Release 2016;237:89–100.

Clémençon B, Babot M, Trézéguet V. The mitochondrial ADP/ATP carrier (SLC25 family): pathological implications of its dysfunction. Mol Aspects Med 2013;34:485–93.

Coppé JP, Rodier F, Patil CK, Freund A, Desprez PY, Campisi J. Tumor suppressor and aging biomarker p16(INK4a) induces cellular senescence without the associated inflammatory secretory phenotype. J Biol Chem 2011;286:36396–403.

Demaria M, Ohtani N, Youssef SA, Rodier F, Toussaint W, Mitchell JR, et al. An essential role for senescent cells in optimal wound healing through secretion of PDGF-AA. Dev Cell 2014;31:722–33.

Detienne G, Van de Walle P, De Haes W, Schoofs L, Temmerman L. SKN-1-independent transcriptional activation of glutathione S-transferase 4 (GST-4) by EGF signaling. Worm 2016;5:e1230585.

Ding X, Kakanj P, Leptin M, Eming SA. Regulation of the wound healing response during aging. J Invest Dermatol 2021;141:1063–70.

Dobin A, Davis CA, Schlesinger F, Drenkow J, Zaleski C, Jha S, et al. STAR: ultrafast universal RNA-seq aligner. Bioinformatics 2013;29:15–21.

Dunn L, Prosser HC, Tan JT, Vanags LZ, Ng MK, Bursill CA. Murine model of wound healing. J Vis Exp 2013;75:e50265.

Ellis S, Lin EJ, Tartar D. Immunology of wound healing. Curr Dermatol Rep 2018;7:350–8.

Fan Y, Cheng J, Zeng H, Shao L. Senescent cell depletion through targeting BCL-family proteins and mitochondria. Front Physiol 2020;11:593630.

Finley PJ, Huckfeldt RE, Walker KD, Shornick LP. Silver dressings improve diabetic wound healing without reducing bioburden. Wounds 2013;25:293–301.

Fleischer JG, Schulte R, Tsai HH, Tyagi S, Ibarra A, Shokhirev MN, et al. Predicting age from the transcriptome of human dermal fibroblasts. Genome Biol 2018;19:221.

Franco AC, Aveleira C, Cavadas C. Skin senescence: mechanisms and impact on whole-body aging. Trends Mol Med 2022;28:97–109.

Freund A, Orjalo AV, Desprez PY, Campisi J. Inflammatory networks during cellular senescence: causes and consequences. Trends Mol Med 2010;16:238–46.

Fu H, Zhou H, Yu X, Xu J, Zhou J, Meng X, et al. Wounding triggers MIRO-1 dependent mitochondrial fragmentation that accelerates epidermal wound closure through oxidative signaling. Nat Commun 2020;11:1050.

Giraud S, Bonod-Bidaud C, Wesolowski-Louvel M, Stepien G. Expression of human ANT2 gene in highly proliferative cells: GRBOX, a new transcriptional element, is involved in the regulation of glycolytic ATP import into mitochondria. J Mol Biol 1998;281:409–18.

Grada A, Otero-Vinas M, Prieto-Castrillo F, Obagi Z, Falanga V. Research techniques made simple: analysis of collective cell migration using the wound healing assay. J Invest Dermatol 2017;137:e11–6.

Harding KG, Moore K, Phillips TJ. Wound chronicity and fibroblast senescence–implications for treatment. Int Wound J 2005;2:364–8.

Harris-Tryon TA, Grice EA. Microbiota and maintenance of skin barrier function. Science 2022;376:940–5.

Hoshino A, Wang WJ, Wada S, McDermott-Roe C, Evans CS, Gosis B, et al. The ADP/ATP translocase drives mitophagy independent of nucleotide exchange. Nature 2019;575:375–9.

Hubackova S, Davidova E, Rohlenova K, Stursa J, Werner L, Andera L, et al. Selective elimination of senescent cells by mitochondrial targeting is regulated by ANT2. Cell Death Differ 2019a;26:276–90.

Hubackova S, Kucerova A, Michlits G, Kyjacova L, Reinis M, Korolov O, et al. IFNgamma induces oxidative stress, DNA damage and tumor cell senescence via TGFβ/SMAD signaling-dependent induction of Nox4 and suppression of ANT2. Oncogene 2016;35:1236–49.

Hubackova S, Magalhaes Novais S, Davidova E, Neuzil J, Rohlena J. Mitochondria-driven elimination of cancer and senescent cells. Biol Chem 2019b;400:141–8.

Jacquier-Sarlin MR, Fuller K, Dinh-Xuan AT, Richard MJ, Polla BS. Protective effects of hsp70 in inflammation. Experientia 1994;50:1031–8.

Jang JY, Choi Y, Jeon YK, Kim CW. Suppression of adenine nucleotide translocase-2 by vector-based siRNA in human breast cancer cells induces apoptosis and inhibits tumor growth in vitro and in vivo. Breast Cancer Res 2008;10:R11.

Jeong HS, Choi HY, Lee ER, Kim JH, Jeon K, Lee HJ, et al. Involvement of caspase-9 in autophagy-mediated cell survival pathway. Biochim Biophys Acta 2011;1813:80–90.

Jiang T, Wang X, Wu W, Zhang F, Wu S. Let-7c miRNA inhibits the proliferation and migration of heat-denatured dermal fibroblasts through down-regulating HSP70. Mol Cells 2016;39:345–51.

Kataoka K, Bilkei-Gorzo A, Nozaki C, Togo A, Nakamura K, Ohta K, et al. Age-dependent alteration in mitochondrial dynamics and autophagy in hippocampal neuron of cannabinoid CB1 receptor-deficient mice. Brain Res Bull 2020;160:40–9.

Kim HS, Je JH, Son TG, Park HR, Ji ST, Pokharel YR, et al. The hepatoprotective effects of adenine nucleotide translocator-2 against aging and oxidative stress. Free Radic Res 2012;46:21–9.

Kirkland JL, Tchkonia T. Cellular senescence: a translational perspective. EBiomedicine 2017;21:21–8.

Ko HJ, Kim J, Ahn M, Kim JH, Lee GS, Shin T. Ergothioneine alleviates senescence of fibroblasts induced by UVB damage of keratinocytes via activation of the Nrf2/HO-1 pathway and HSP70 in keratinocytes. Exp Cell Res 2021;400:112516.

Kotwal GJ, Chien S. Macrophage differentiation in normal and accelerated wound healing. Results Probl Cell Differ 2017;62:353–64.

Kovalchin JT, Wang R, Wagh MS, Azoulay J, Sanders M, Chandawarkar RY. In vivo delivery of heat shock protein 70 accelerates wound healing by up-regulating macrophage-mediated phagocytosis. Wound Repair Regen 2006;14:129–37.

Lakhani SA, Masud A, Kuida K, Porter GA Jr, Booth CJ, Mehal WZ, et al. Caspases 3 and 7: key mediators of mitochondrial events of apoptosis. Science 2006;311:847–51.

Lee TY. Lactate: a multifunctional signaling molecule. Yeungnam Univ J Med 2021;38:183–93.

Love MI, Huber W, Anders S. Moderated estimation of fold change and dispersion for RNA-seq data with DESeq2. Genome Biol 2014;15:550.

Maxson S, Lopez EA, Yoo D, Danilkovitch-Miagkova A, Leroux MA. Concise review: role of mesenchymal stem cells in wound repair. Stem Cells Transl Med 2012;1:142–9.

Mintie CA, Singh CK, Ahmad N. Whole fruit phytochemicals combating skin damage and carcinogenesis. Transl Oncol 2020;13:146–56.

Mishra P, Chan DC. Metabolic regulation of mitochondrial dynamics. J Cell Biol 2016;212:379–87.

Pak O, Sommer N, Hoeres T, Bakr A, Waisbrod S, Sydykov A, et al. Mitochondrial hyperpolarization in pulmonary vascular remodeling. Mitochondrial uncoupling protein deficiency as disease model. Am J Respir Cell Mol Biol 2013;49:358–67.

Pan T, Liu J, Xu S, Yu Q, Wang H, Sun H, et al. ANKRD22, a novel tumor microenvironment-induced mitochondrial protein promotes metabolic reprogramming of colorectal cancer cells. Theranostics 2020;10:516–36.

Passos JF, von Zglinicki T. Methods for cell sorting of young and senescent cells. Methods Mol Biol 2007;371:33–44.

Pedersen PL. Tumor mitochondria and the bioenergetics of cancer cells. Prog Exp Tumor Res 1978;22:190–274.

Prahl S, Kueper T, Biernoth T, Wöhrmann Y, Münster A, Fürstenau M, et al. Aging skin is functionally anaerobic: importance of coenzyme Q10 for anti aging skin care. BioFactors 2008;32:245–55.

Ravera S, Podestà M, Sabatini F, Dagnino M, Cilloni D, Fiorini S, et al. Discrete changes in glucose metabolism define aging. Sci Rep 2019;9:10347.

Reinke JM, Sorg H. Wound repair and regeneration. Eur Surg Res 2012;49:35–43.

Rellmann Y, Dreier R. Different forms of ER stress in chondrocytes result in short stature disorders and degenerative cartilage diseases: new insights by cartilage-specific ERp57 knockout mice. Oxid Med Cell Longev 2018;2018:8421394.

Samdavid Thanapaul RJR, Shvedova M, Shin GH, Crouch J, Roh DS. Elevated skin senescence in young mice causes delayed wound healing. GeroScience 2022;44:1871–8.

Schniertshauer D, Gebhard D, Bergemann J. Age-dependent loss of mitochondrial function in epithelial tissue can be reversed by coenzyme Q10. J Aging Res 2018;2018:6354680.

Seliger C, Leukel P, Moeckel S, Jachnik B, Lottaz C, Kreutz M, et al. Lactate-modulated induction of THBS-1 activates transforming growth factor (TGF)-beta2 and migration of glioma cells in vitro [published correction appears in PLoS One 2014;9] PLoS One 2014;8:e78935.

Sindrilaru A, Peters T, Wieschalka S, Baican C, Baican A, Peter H, et al. An unrestrained proinflammatory M1 macrophage population induced by iron impairs wound healing in humans and mice. J Clin Invest 2011;121:985–97.

Soto-Heredero G, Gómez de Las Heras MM, Gabandé-Rodríguez E, Oller J, Mittelbrunn M. Glycolysis - a key player in the inflammatory response. FEBS J 2020;287:3350–69.

Stadelmann WK, Digenis AG, Tobin GR. Physiology and healing dynamics of chronic cutaneous wounds. Am J Surg 1998;176:26S–38S.

Stuhldreier F, Kassel S, Schumacher L, Wesselborg S, Proksch P, Fritz G. Pleiotropic effects of spongean alkaloids on mechanisms of cell death, cell cycle progression and DNA damage response (DDR) of acute myeloid leukemia (AML) cells. Cancer Lett 2015;361:39–48.

Subramanian A, Tamayo P, Mootha VK, Mukherjee S, Ebert BL, Gillette MA, et al. Gene set enrichment analysis: a knowledge-based approach for interpreting genome-wide expression profiles. Proc Natl Acad Sci USA 2005;102:15545–50.

Truschel ST, Clayton DR, Beckel JM, Yabes JG, Yao Y, Wolf-Johnston A, et al. Age-related endolysosome dysfunction in the rat urothelium. PLoS One 2018;13:e0198817.

Tubita A, Lombardi Z, Tusa I, Lazzeretti A, Sgrignani G, Papini D, et al. Inhibition of ERK5 elicits cellular senescence in melanoma via the cyclin-dependent kinase inhibitor p21. Cancer Res 2022;82:447–57.

Virag JA, Rolle ML, Reece J, Hardouin S, Feigl EO, Murry CE. Fibroblast growth factor-2 regulates myocardial infarct repair: effects on cell proliferation, scar contraction, and ventricular function. Am J Pathol 2007;171:1431–40.

Waldera Lupa DM, Kalfalah F, Safferling K, Boukamp P, Poschmann G, Volpi E, et al. Characterization of skin aging-associated secreted proteins (SAASP) produced by dermal fibroblasts isolated from intrinsically aged human skin. J Invest Dermatol 2015;135:1954–68.

Wall IB, Moseley R, Baird DM, Kipling D, Giles P, Laffafian I, et al. Fibroblast dysfunction is a key factor in the non-healing of chronic venous leg ulcers. J Invest Dermatol 2008;128:2526–40.

Wang J, Zhang Q, Wan R, Mo Y, Li M, Tseng MT, et al. Intracellular adenosine triphosphate delivery enhanced skin wound healing in rabbits. Ann Plast Surg 2009;62:180–6.

Wang L, Schumann U, Liu Y, Prokopchuk O, Steinacker JM. Heat shock protein 70 (Hsp70) inhibits oxidative phosphorylation and compensates ATP balance through enhanced glycolytic activity. J Appl Physiol (1985) 2012;113:1669–76.

Wang Z, Shi C. Cellular senescence is a promising target for chronic wounds: a comprehensive review. Burns Trauma 2020;8:tkaa021.

Yoo H, Kang JW, Lee DW, Oh SH, Lee YS, Lee EJ, et al. Pyruvate metabolism: A therapeutic opportunity in radiation-induced skin injury. Biochem Biophys Res Commun 2015;460:504–10.

Yosefzon Y, Soteriou D, Feldman A, Kostic L, Koren E, Brown S, et al. Caspase-3 regulates YAP-dependent cell proliferation and organ size. Mol Cell 2018;70:573–87.e4.

Zhai L, Xu X, Liu J, Jing C, Yang X, Zhao D, et al. A novel biochemical study of anti-dermal fibroblast replicative senescence potential of *Panax notoginseng* oligosaccharides. Front Pharmacol 2021;12:690538.

Zheng Q, Huang C, Guo J, Tan J, Wang C, Tang B, et al. Hsp70 participates in PINK1-mediated mitophagy by regulating the stability of PINK1. Neurosci Lett 2018;662:264–70.

SUPPLEMENTARY MATERIALS AND METHODS

Production of lentiviral particles for protein overexpression

Human ANT2-open reading frame (NM_001152, OriGene, Rockville, USA) and mouse ANT2-open reading frame (NM_007451, OriGene) clones were amplified with Stbl3 competent *E. coli* and confirmed by sequencing. The genes were subcloned into a pLenti6.3/V5 plasmid (Invitrogen, Waltham, MA) with FLAG, Myc, and V5 tags that were distinguishable from those of the control vector marker.

The viruses were produced in human embryonic kidney 293T cells. Cells (8×10^6) were plated in T75 flasks 1 day before transfection with 10 μg of each open reading frame–containing plasmids, VSV.G and PAX2, using Lipofectamine 2000 as the transfection reagent (11668-019, Invitrogen) mixed at a 1:2 ratio with Opti-MEM (11058-021, Gibco, Grand Island, NY). Fresh DMEM containing 5 mM sodium butyrate (B5887,Sigma-Aldrich, St. Louis, MO) was changed within 15 hours, and medium containing viral particles was harvested twice every 24 hours. After concentration with a Lenti-X Concentrator (number 631232, Takara Bio, Otsu, Japan), the viral particles were diluted in Dubellco's PBS (LB 001-02, WELGENE, Gyeongsan, Korea) and stored at −80 °C.

Histological and immunohistochemical analysis

In human skin samples, immunohistochemical staining of the formalin-fixed, paraffin-embedded tissue sections (4-μm thick) for ANT2 expression detection was performed with a Benchmark XT automated immunohistochemistry stainer (Ventana Medical Systems, Tucson, AZ). A primary anti-ANT2 antibody (MBS540797, MyBioSource, San Diego, CA) was used. Detection was performed with an UltraView Universal Alkaline Phosphatase Red Detection kit (Roche Diagnostics, Basel, Switzerland). This study was approved by the institutional review board of Ajou University Hospital (Suwon, South Korea) (AJIRB-BMR-SMP-17-438).

Mouse skin samples were collected and immediately cut in half vertically. The samples were fixed overnight with formalin (HT501128, Sigma-Aldrich) and embedded in paraffin (Kyungpook National University Hospital BMRI, Daegu, Korea). Paraffin sections (approximately 4-μm thick) were used for histological analysis after H&E, Masson's trichrome, or immunohistochemical staining for F4/80 (sc-52664, Santa Cruz Biotechnology, Dallas, TX), Ly-6G/Ly-6C (14-59321-82, Invitrogen), Ki-67 (MA5-14520, Invitrogen), and CD31 (ab28364, Abcam, Cambridge, United Kingdom) at Histoire (Seoul, Korea) and counterstained with H&E. The immunoreactions were visualized under a microscope (Stereo Investigator, Carl Zeiss, Jena, Germany), and the images were quantified using an immunohistochemical image analysis toolbox in ImageJ software (Shu et al., 2013). The number of counted cells (positively stained cells) was normalized per view field.

Immunofluorescence

Paraffin sections on slides were deparaffinized in a graded series of xylene (534056, Sigma-Aldrich) and ethanol (UN1170, Duksan, Seoul, Korea). The slides were incubated in 1 mM EDTA buffer (pH 8.0, E522, VWR International, Radnor, PA) at 100 °C for 10 minutes for antigen retrieval (heat-induced epitope retrieval) followed by permeabilization in 0.25% Triton-X 100 for 10 minutes. Then, the slides were incubated with primary antibodies against mCherry (1:300, ab167453, Abcam) or Myc-tag (1:200–1:800, C3956, Sigma-Aldrich), and the immunoactivity was detected with a Cy3 anti-rabbit IgG (1:100, 711-165-152, Jackson Immuno Research Laboratories, West Grove, PA) secondary antibody. The sections were counterstained with DAPI (H-1200, Vector Laboratories, Burlingame, CA), and the immunoreactions were visualized with an imaging microscope (AXIO Observer, Carl Zeiss).

Analysis of mitochondrial morphology and function

To visualize the mitochondrial morphology, LacZ-overexpressing (as a control) or ANT2-overexpressing senescent human dermal fibroblasts (HDFs) were cultured in six-well plates. The cells were stained with MitoTracker deep red (10 μM, 1:500, Thermo Fisher Scientific, Waltham, MA) and Hoechst 33342 (10 μg/ml, 1:20,000) for 30 minutes. The cells were observed with a fluorescence microscope (AXIO Observer, Carl Zeiss) at low magnification (×40) or a confocal microscope (High-Resolution Live Cell Imaging System - FV1200, Olympus, Tokyo, Japan) at high magnification (×1,000). The mitochondrial area was analyzed using the ImageJ method with the specifications—eight-bit image, contrast limited adaptive histogram equalization, tubeness value = 1.5—and then converted into binary images (Bosch and Calvo, 2019).

To examine mitochondrial function, flow cytometry analysis was carried out. Briefly, LacZ-overexpressing (control) or ANT2-overexpressing HDFs were plated in 60-mm dishes and allowed to grow to 85% confluence. After washing with Dubellco's PBS, the cells were incubated with MitoTracker deep red (100 nM, Thermo Fisher Scientific) to estimate mitochondrial density, MitoSOX (5 μM, Thermo Fisher Scientific) to measure the amount of mitochondrial superoxide, or tetramethylrhodamine methyl ester (100 nM, Thermo Fisher Scientific) to measure the mitochondrial membrane potential for 30 minutes at 37 °C. After staining, the fluorescence intensity from a single cell was measured with an LSRFortessa (BD Biosciences, San Jose, CA) flow cytometer. The tetramethylrhodamine methyl ester intensity of each population was normalized to that of MitoTracker. In addition, after this assay, the values of forward scatter (cell size), side scatter (cell granulation), and FITC (autofluorescence of lipofuscin) were acquired. To measure the mitochondrial permeability transition pore opening, a MitoProbe Transition Pore Assay Kit (M34153, Thermo Fisher Scientific) was used according to the manufacturer's instructions. Specifically, LacZ-overexpressing (control) and ANT2-overexpressing HDFs were harvested as described earlier. The samples were treated as follows: group I (calcein), group II (calcein + cobalt chloride), and group III (calcein + cobalt chloride + ionomycin). Cells were stained with calcein AM (2 μM), cobalt chloride (80 mM), and ionomycin (100 μM) in 1× Hank's balanced salt solution (LB203-04, WELGENE) for 15 minutes at room temperature. The change in fluorescence intensity between groups II and III, indicating continuous activation of the mitochondrial permeability transition pore, was measured by flow cytometry analysis.

Western blot analysis

Cells were lysed in an SDS sample buffer containing Tris-hydrogen chloride (pH 6.8), 50% glycerol, 10% SDS, β-mercaptoethanol, and 1% bromophenol blue. The tissues were homogenized in RIPA buffer (RC2002-050-00, Biosesang, Yongin, South Korea) that included a proteinase inhibitor (1862209, Thermo Fisher Scientific), phosphatase inhibitor (1862495, Thermo Fisher Scientific), and 5× sample buffer. The lysed samples were boiled at 95 °C for 5 minutes and stored at −20 °C. After protein quantification with protein assay reagents (numbers 5000114, 5000113, and 5000115, Bio-Rad Laboratories, Hercules, CA), the solubilized proteins (30−40 μg) from the cells and tissues were separated by SDS-PAGE (10−15% gel, depending on the molecular weight of the target protein) and then transferred onto a nitrocellulose membrane (number 10600003, Amersham Pharmacia Biotech, Amersham, United Kingdom). The membrane was blocked with 5% BSA (100-10SB, LEE BioSolutions, Maryland Heights, MO) diluted in Tris-buffered saline containing 0.05% Tween-20 for 1 hour and then incubated with primary antibodies overnight. Next, the membrane was incubated with horseradish peroxidase−conjugated secondary antibodies. Immunoreactive proteins were visualized by chemiluminescence (number P90720, MilliporeSigma, Burlington, MA) with an ImageQuant LAS-4000 digital imaging system (GE Healthcare, Milwaukee, WI). Protein bands were quantified using Image Quant TL software 8.1.

The primary antibodies used for western blotting were as follows: anti-ANT2 (1:1,000, E2BD, Cell Signaling Technology, Danvers, MA), anti-ANT2 (1:1,000, provided in Pusan National University, Busan, South Korea), anti−α-tubulin (1:4,000, T5168, Sigma-Aldrich), anti-p16 (1:1,000, ab108349, Abcam), anti−β-actin (1:50,000, A1978, Sigma-Aldrich), anti-Flag (1:1,000, A8592, Sigma-Aldrich), anti-pH3S10 (1:1,000, 9701S, Cell Signaling Technology), anti-p21 (1:1,000, 2947S, Cell Signaling Technology), anti-p62 (1:1,000, P0067, Sigma-Aldrich), anti-Parkin (1:200, sc-32282, Santa Cruz Biotechnology), anti-PINK1 (1:1,000, BC100-494, Novus Biologicals, Centennial, CO), anti-HSPA6 (1:1,000, ab69408, Abcam), anti-Caspase-3 (D3R6Y) (1:1,000, number 14220, Cell Signaling Technology), anti-Caspase-7 (D2Q3L) (1:1,000, number 12827, Cell Signaling Technology), anti-Caspase-9 (1:1,000, number 9508, Cell Signaling Technology), anti-PDHA1 (phosphorylated S293) (1:1,000, ab92696, Abcam), and anti-PDHA1 antibody (9H9AF5) (1:1,000, ab110330, Abcam). Secondary antibodies used included anti-rabbit IgG, horseradish peroxidase−linked (1:1,000, number 7074, Cell Signaling Technology); anti-rabbit IgG, horseradish peroxidase−linked (1:5,000, Jackson ImmunoResearch, West Grove, PA); and anti-mouse IgG, horseradish peroxidase−linked (1:5,000, Jackson ImmunoResearch).

RT-qPCR

Total RNA was isolated from cells and mouse skin samples, as described earlier. cDNA was synthesized using Transcriptor First Strand cDNA Synthesis Kit (04 896 866 01, Roche Diagnostics). Real-time PCR was performed with KAPA SYBR FAST qPCR Master Mix (2×) Kit (07959397001, Sigma-Aldrich) on a Light Cycler 480 II detection system (Roche Diagnostics). PCR was performed using the following parameters: 95 °C for 5 minutes, 45 cycles of 95 °C for 10 seconds, 60 °C for 10 seconds, and 72 °C for 10 seconds, followed by 95 °C for 5 seconds and 65 °C for 1 minute. The relative expression of each target gene was calculated through the comparative Ct method. The mRNA expression levels of *GAPDH* and *RPS11* were used as the internal controls for normalization. The primers used for the RT-PCR are listed in Supplementary Table S1.

RNA interference

RNA interference experiments were performed using HDFs. Complementary RNA oligonucleotides were derived from HSPA6 cDNA (AccuTarget Genome-wide Predesigned siRNA, 10 nmol, BioRP, Bioneer, Daejeon, South Korea). A pair of nonspecific scrambled RNA oligonucleotides (Bioneer) was used as a control. Transfection was performed once mCherry-overexpressing (control) and ANT2-overexpressing senescent HDFs reached 80% confluence in six-well plates. The cells were treated with a mixture containing a short interfering RNA duplex (30 μM) and Lipofectamine RNAiMAX (13778-500, Invitrogen) in Opti-MEM for 48 hours at 37 °C. Then, the medium was replaced with fresh DMEM, and the cells were harvested 24 hours later for subsequent experiments.

ELISA

Skin samples were collected from mice injected with lentiviral particles containing the mCherry (control) or ANT2 gene on day 7. Proteins were extracted from the dissected mouse skin samples with lysis buffer on ice, as described in the western blot analysis section. The concentration of TNFα was measured with a mouse ELISA kit (R&D Systems, Minneapolis, MN) according to the manufacturer's instructions.

SUPPLEMENTARY REFERENCES

Ahlers JMD, Falckenhayn C, Holzscheck N, Solé-Boldo L, Schütz S, Wenck H, et al. Single-cell RNA profiling of human skin reveals age-related loss of dermal sheath cells and their contribution to a juvenile phenotype. Front Genet 2022;12:797747.

Aramillo Irizar P, Schäuble S, Esser D, Groth M, Frahm C, Priebe S, et al. Transcriptomic alterations during ageing reflect the shift from cancer to degenerative diseases in the elderly [published correction appears in Nat Commun 2019;10:2459] Nat Commun 2018;9:327.

Bosch A, Calvo M. Automated Quantitative Analysis of Mitochondrial Morphology. Methods Mol Biol 2019;2040:99−115.

Fleischer JG, Schulte R, Tsai HH, Tyagi S, Ibarra A, Shokhirev MN, et al. Predicting age from the transcriptome of human dermal fibroblasts. Genome Biol 2018;19:221.

Shu J, Fu H, Qiu G, Kaye P, Ilyas M. Segmenting overlapping cell nuclei in digital histopathology images. Annu Int Conf IEEE Eng Med Biol Soc 2013;2013:5445−8.

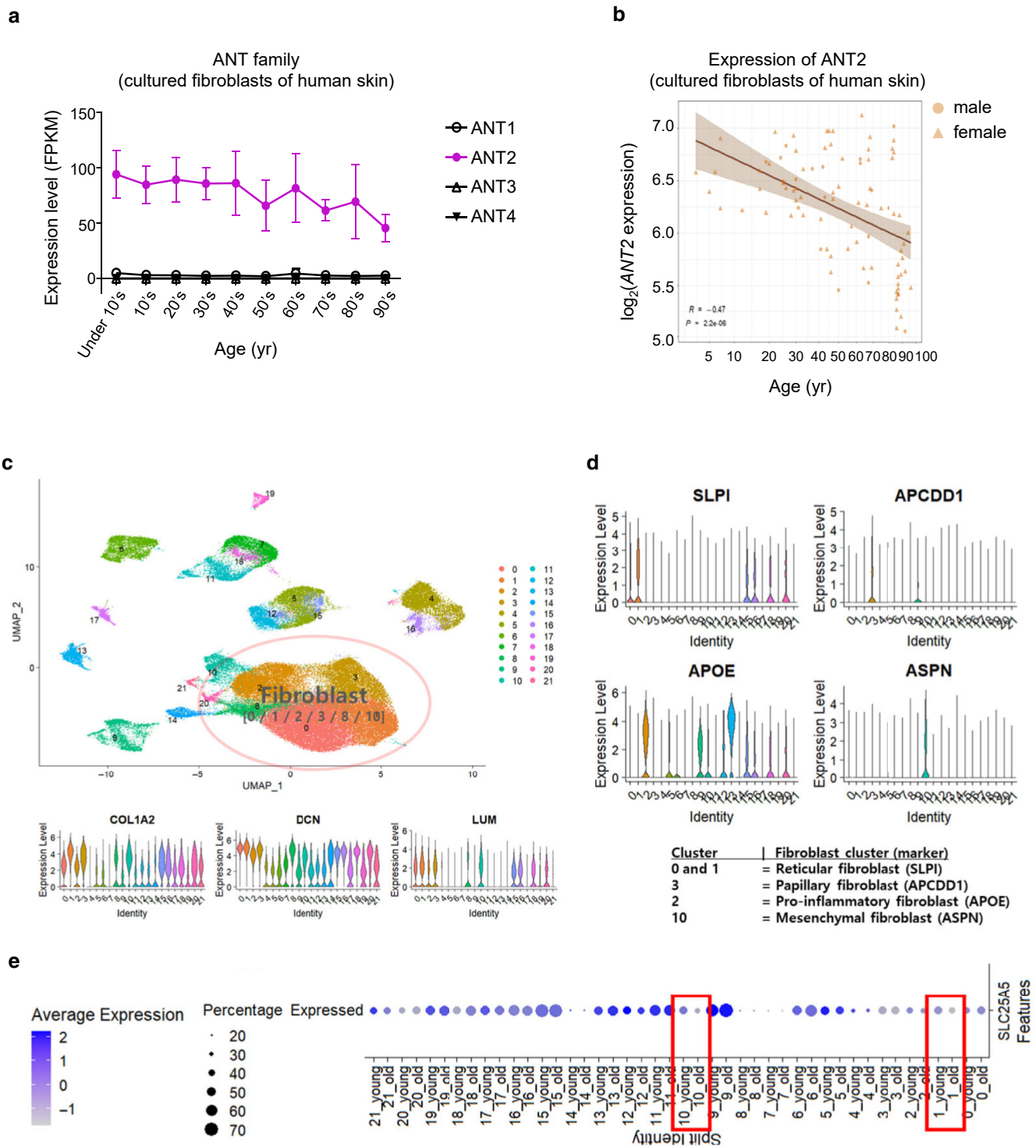

Supplementary Figure S1. Downregulation of ANT2 expression in aging. (**a**) Changes in the expression of ANT family mRNA with age. (**b**) Scatter plot showing the *ANT2* mRNA expression pattern in cultured fibroblasts from human skin. The Pearson-R value in the graph shows gene expression and age across all samples. The circles represent samples from males, and the triangles represent samples from females. The brown line denotes the regression line for the samples. (**a, b**) Public skin-aging RNA-seq data (Fleischer et al., 2018) were analyzed. (**c**) UMAP plot of the single-cell RNA-seq data (Ahlers et al., 2022) with 21 cell clusters identified. The bottom panel displays the expression of fibroblast markers in each of the 21 cell clusters. Cell clusters 0, 1, 2, 3, 8, and 10 were identified as fibroblast cells. (**d**) Violin plot of the expression of fibroblast markers in each of the four subclusters: reticular, papillary, proinflammatory, and mesenchymal. Cell clusters 0 and 1 were assigned to reticular fibroblasts, cell cluster 3 was assigned to papillary fibroblasts, cell cluster 2 was assigned to proinflammatory fibroblasts, and cell cluster 10 was assigned to mesenchymal fibroblasts on the basis of the expression of specific markers. (**e**) Dot plot comparing the expression of *ANT2* between young and old groups in each cell-type cluster. In clusters 1 (reticular) and 10 (mesenchymal) (red boxes), *ANT2* expression is decreased in the aged group. (**f**) IHC staining of ANT2 in young (top) and old (bottom) skin tissue sections from subjects aged 28 years and 68 years. The arrow indicates stained cells in the dermis. Bar = 100 μm. (**g**) Immunoblots and quantification of ANT2 expression in nonsenescent or senescent HDFs. The expression level was normalized to that of β-actin (loading control). The data are shown as the mean ± SD; n (biological replicate) = 3. (**h**) Box and

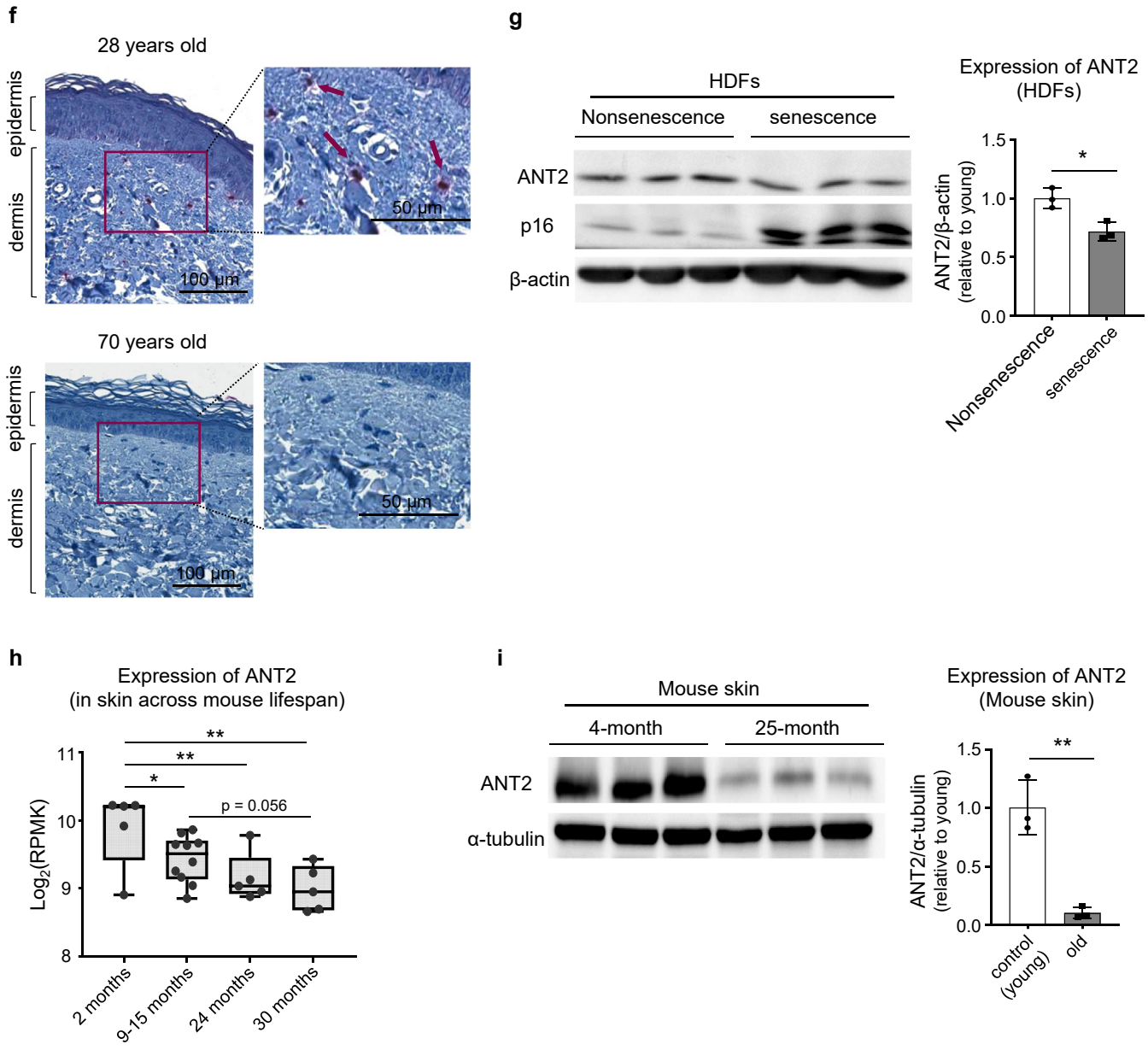

Supplementary Figure S1. Continued.

whisker plot showing the *Ant2* expression pattern in mouse skin tissue. Public skin-aging RNA-seq data (GSE75192 [Aramillo Irizar et al., 2018]) were analyzed. Transcriptome alterations in four age groups: young (aged 2 months), middle-aged (9−15 months), old (aged 24 months), and oldest old (aged 30 months). (**i**) Immunoblots and quantification of ANT2 expression in the skin of male mice aged 4 and 25 months. The expression level was normalized to that of α-tubulin (loading control) for quantification. The data are shown as the mean ± SD; n (biological replicate) = 3. For the statistical analyses shown in **g** and **i**, $*P \leq 0.05$ and $**P \leq 0.01$, as determined by unpaired *t*-test. For those in **h**, $*P \leq 0.05$ and $**P \leq 0.01$, as determined by one-way ANOVA. ANT, adenine nucleotide translocase; FPKM, fragments per kilobase of transcript per million mapped reads; HDF, human dermal fibroblast; IHC, immunohistochemical; RNA-seq, RNA sequencing; UMAP, Uniform Manifold Approximation and Projection; yr, year.

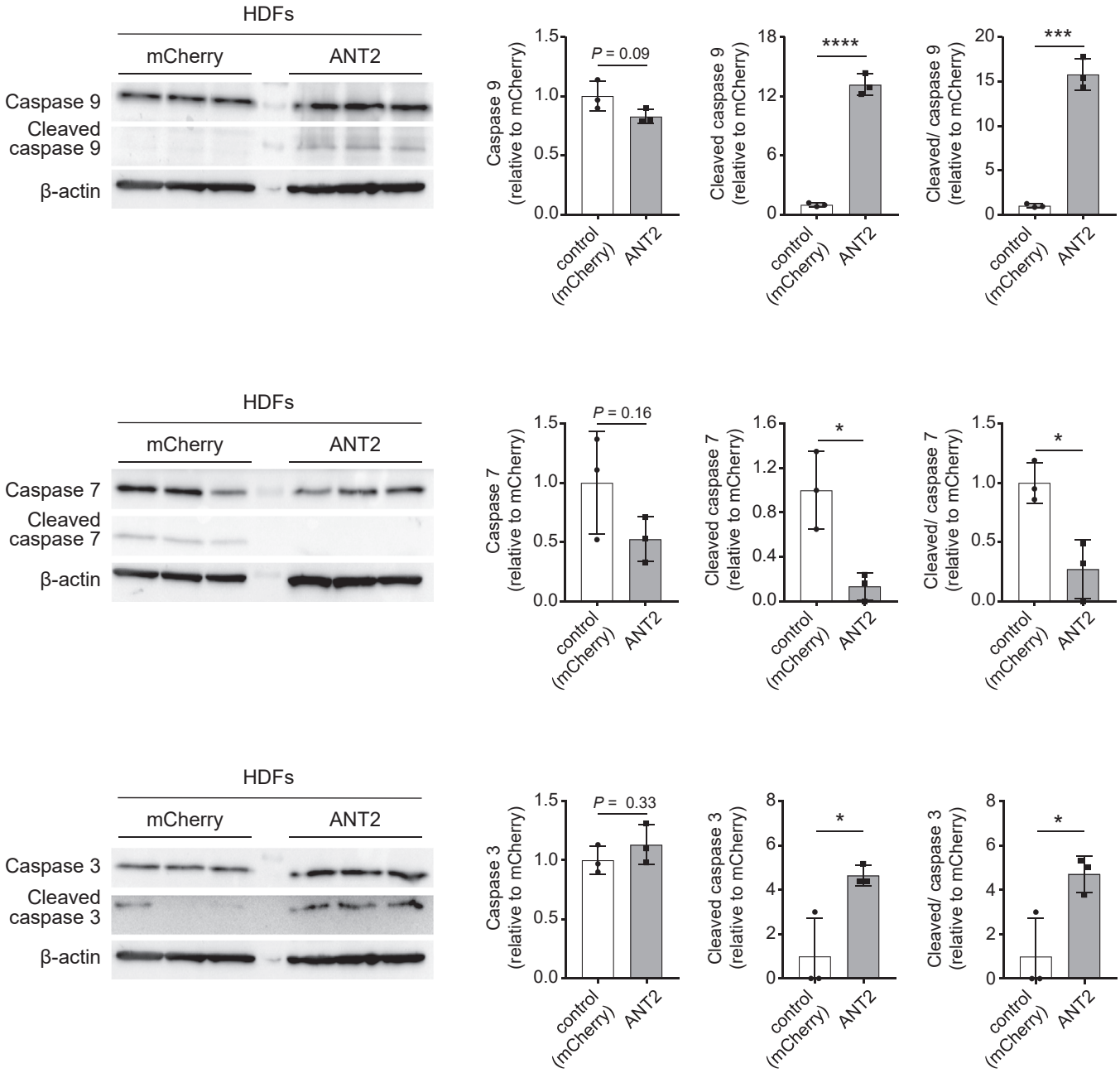

Supplementary Figure S2. ANT2-induced changes of caspase activation in senescent HDFs. Immunoblots and quantification of caspases-9, -7, and -3 in the mCherry-OE (control) and the ANT2-OE senescent HDFs. The expression level was normalized to that of β-actin. The data are shown as the mean ± SD; n (biological replicate) = 3. For statistical analyses, $*P \leq 0.05$, $***P \leq 0.001$, and $****P \leq 0.0001$ as determined by unpaired *t*-test. ANT2-OE, ANT2-overexpressing; HDF, human dermal fibroblast; mCherry-OE, mCherry-overexpressing.

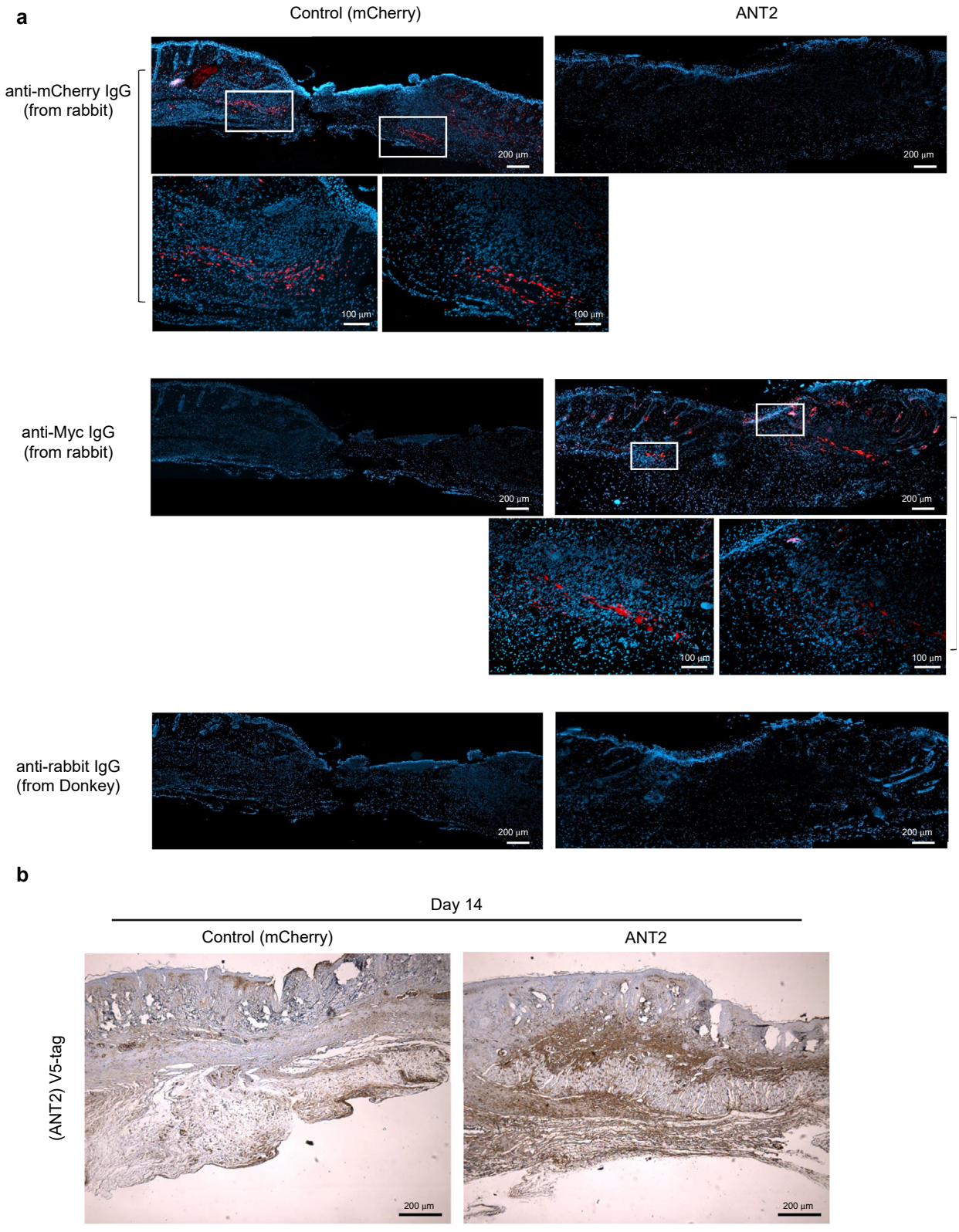

Supplementary Figure S3. Validated ANT2 overexpression in aged mouse skin after lentiviral transduction. (**a**) Immunofluorescence showing ANT2 or mCherry overexpression in mouse skin 7 days after subcutaneous lentiviral injection. DAPI was used for counterstaining. Bar = 200 μm and 100 μm. Continuous images were stitched with ImageJ software. (**b**) Immunohistochemical staining for ANT2 (as V5-tag) in the mCherry-OE (control) and the ANT2-OE mouse skin tissue on day 14 after wounding. Bar = 200 μm. ANT2-OE, ANT2-overexpressing; mCherry-OE, mCherry-overexpressing.

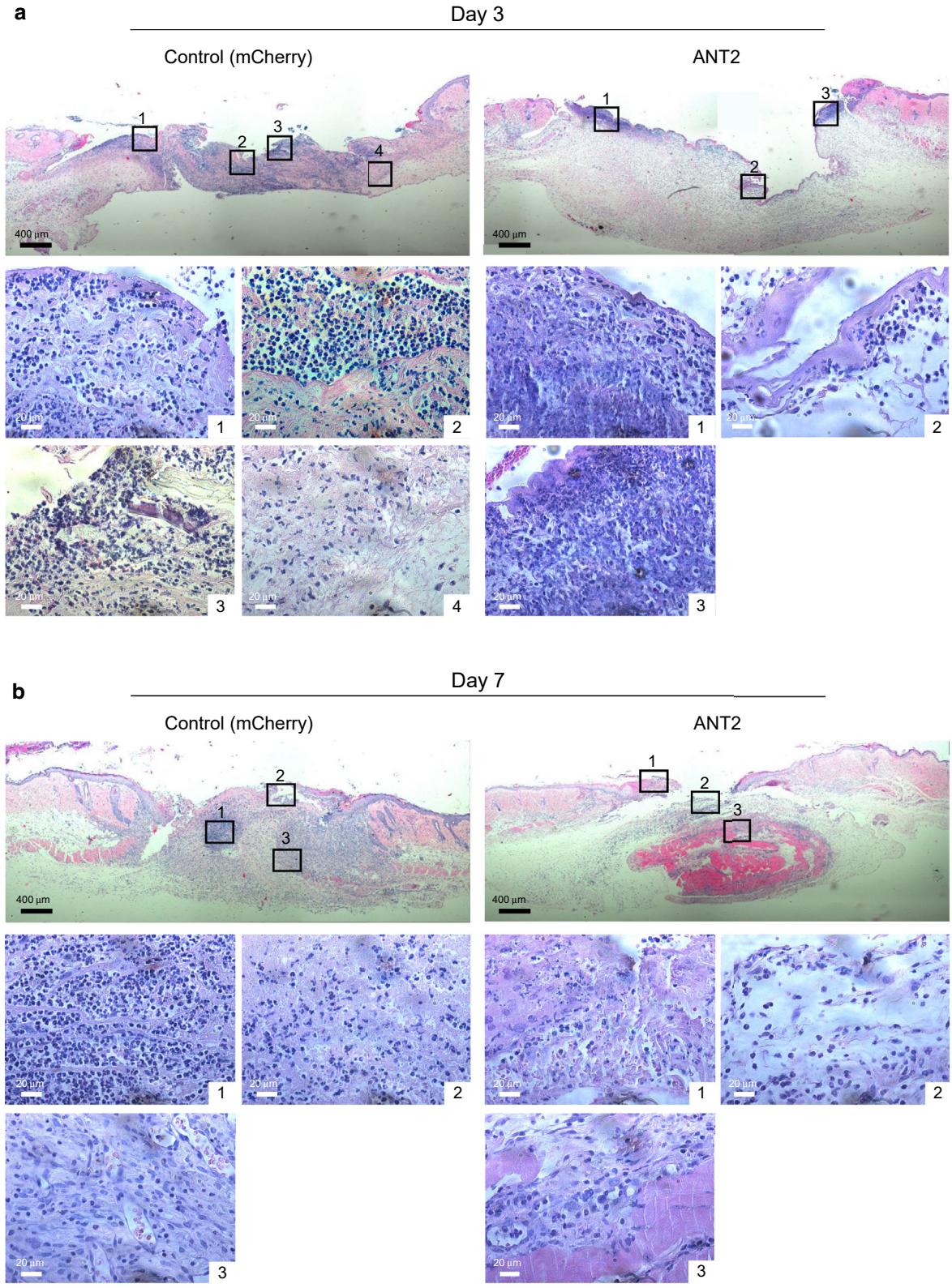

Supplementary Figure S4. Nuclear morphology in ANT2-overexpressing aged mouse skin during wound healing. (**a**–**d**) H&E staining images of major cellular nuclei in a wound site. Bar = 400 μm (top) and bar = 20 μm (bottom) from day 3 to day 14.

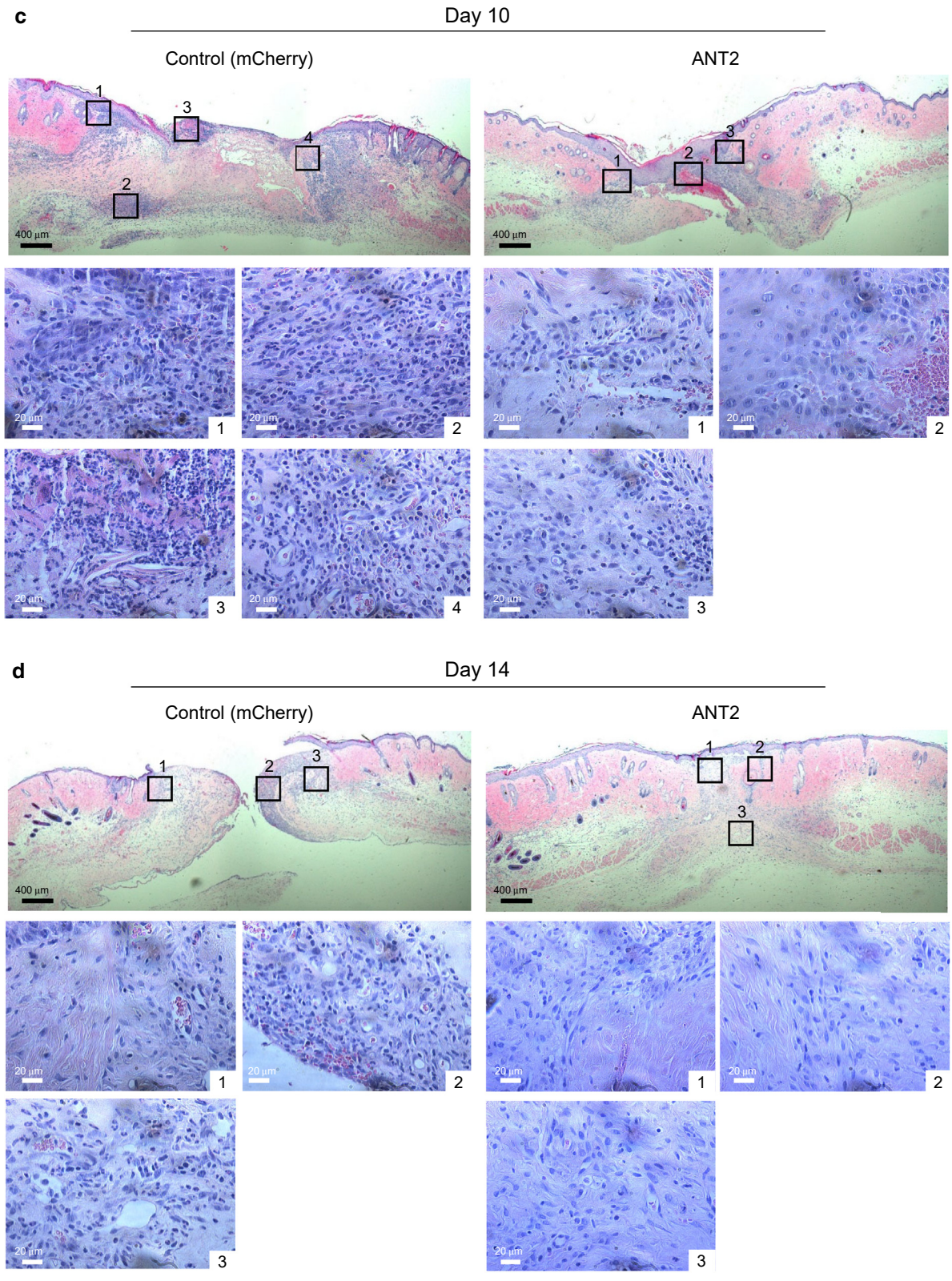

Supplementary Figure S4. Continued.

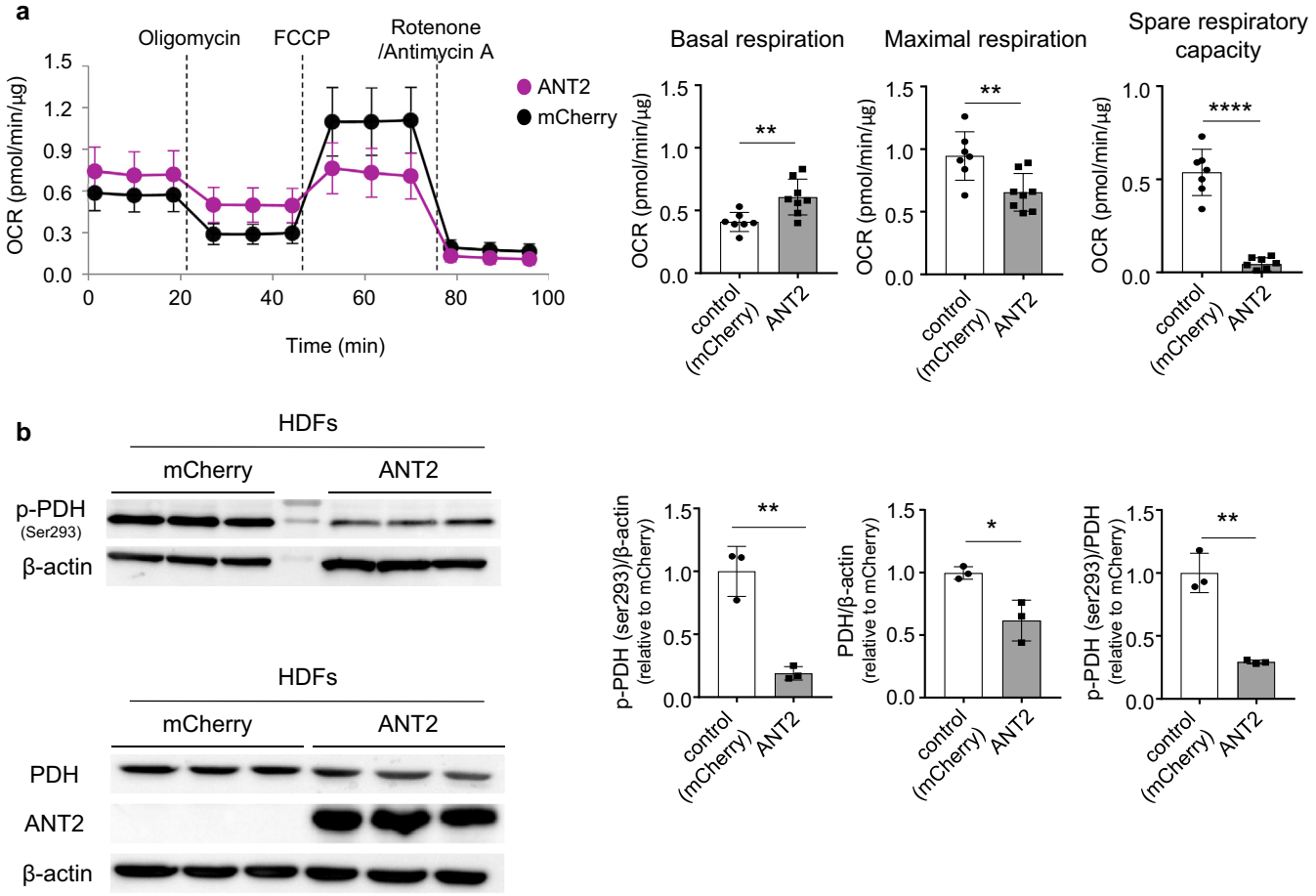

Supplementary Figure S5. ANT2-mediated changes in the OCR and the activation of PDH in senescent HDFs. (**a**) Mitochondrial stress test with monitoring OCR in mCherry-OE (control) and ANT2-OE senescent HDFs. Basal respiration, mitochondrial ATP production, maximal respiration, and spare respiratory capacity were quantified. The black dotted lines indicate when the corresponding chemicals were added to the cells. The data are shown as the mean ± SD; n = 7−8 samples per experiment. (**b**) Immunoblots and quantification for monitoring the activation of PDH in mCherry-OE (control) and ANT2-OE senescent HDFs. HDFs were normalized by β-actin. The data are shown as the mean ± SD; n (biological replicate) = 3. For statistical analyses, $*P \leq 0.05$, $**P \leq 0.01$, and $****P \leq 0.0001$ as determined by unpaired *t*-test. ANT2-OE, ANT2-overexpressing; ATP, adenosine triphosphate; FCCP, carbonyl cyanide 4-(trifluoromethoxy) phenylhydrazone; HDF, human dermal fibroblast; mCherry-OE, mCherry-overexpressing; min, minute; OCR, oxygen consumption rate; PDH, pyruvate dehydrogenase; p-PDH, phosphorylated pyruvate dehydrogenase.

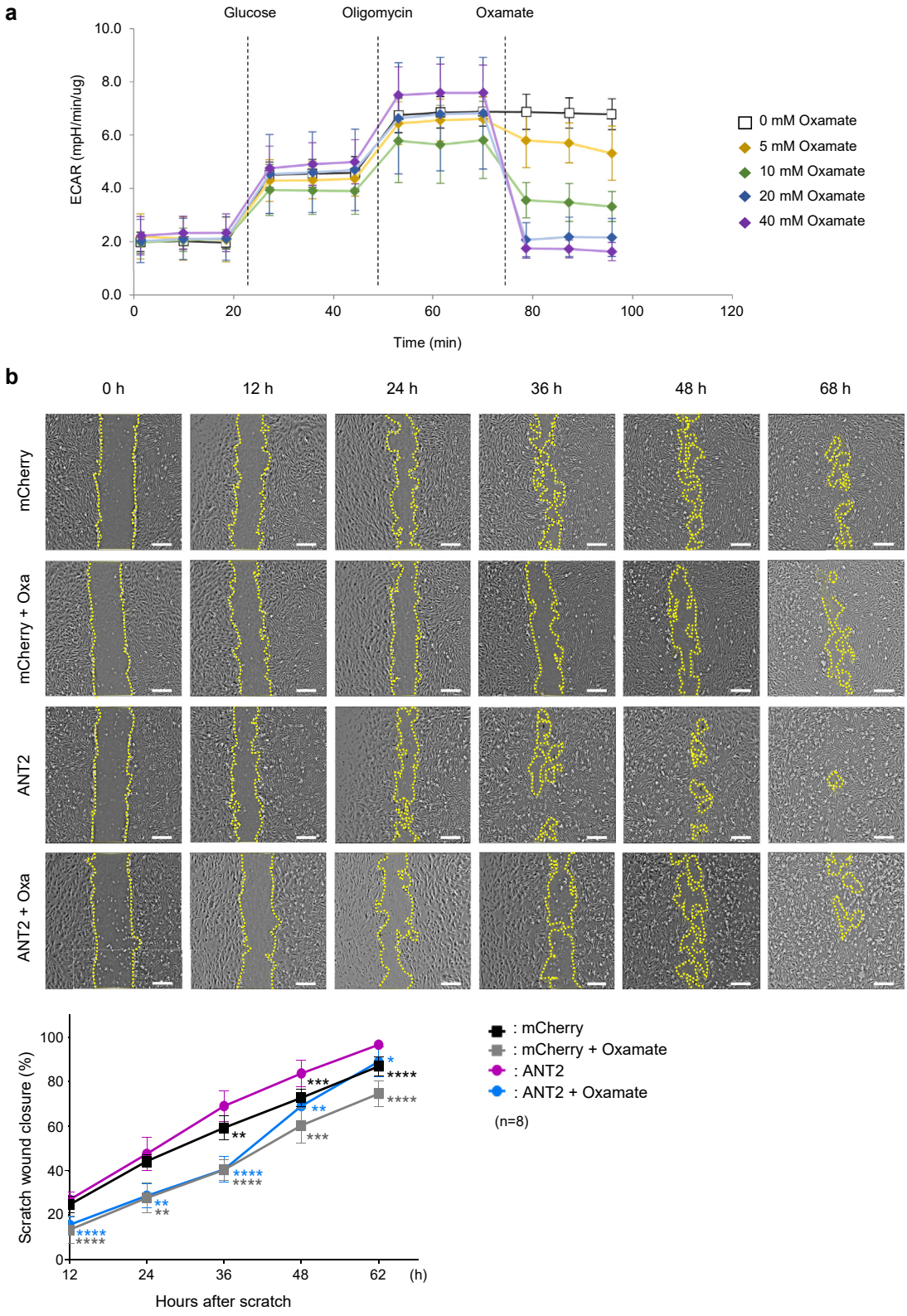

Supplementary Figure S6. The migratory capacity of HDFs as determined by increased glycolysis after ANT2 overexpression in senescent cells. (**a**) The concentration of Oxa, an inhibitor of glycolysis, depends on ECAR changes to determine the optimal dose of the chemical for carrying out a scratch wound healing assay. A total of 20 mM Oxa was used for the experiments. (**b**) Time-lapse images showing wound closure in senescent HDFs 0, 12, 24, 36, 48, and 68 h after scratch. The terminal cell migratory region is indicated by a yellow dotted line. Bar = 500 μm. The migration area was quantified with ImageJ software. The data are shown as the mean ± SD; n (biological replicate) = 8. Significant data are represented as the mean ± SD. For statistical analyses, $*P \leq 0.05$, $**P \leq 0.01$, $***P \leq 0.001$, and $****P \leq 0.0001$ as determined by multiple *t*-tests. ECAR, extracellular acidification rate; h, hour; HDF, human dermal fibroblast; min, minute; Oxa, sodium oxamate.

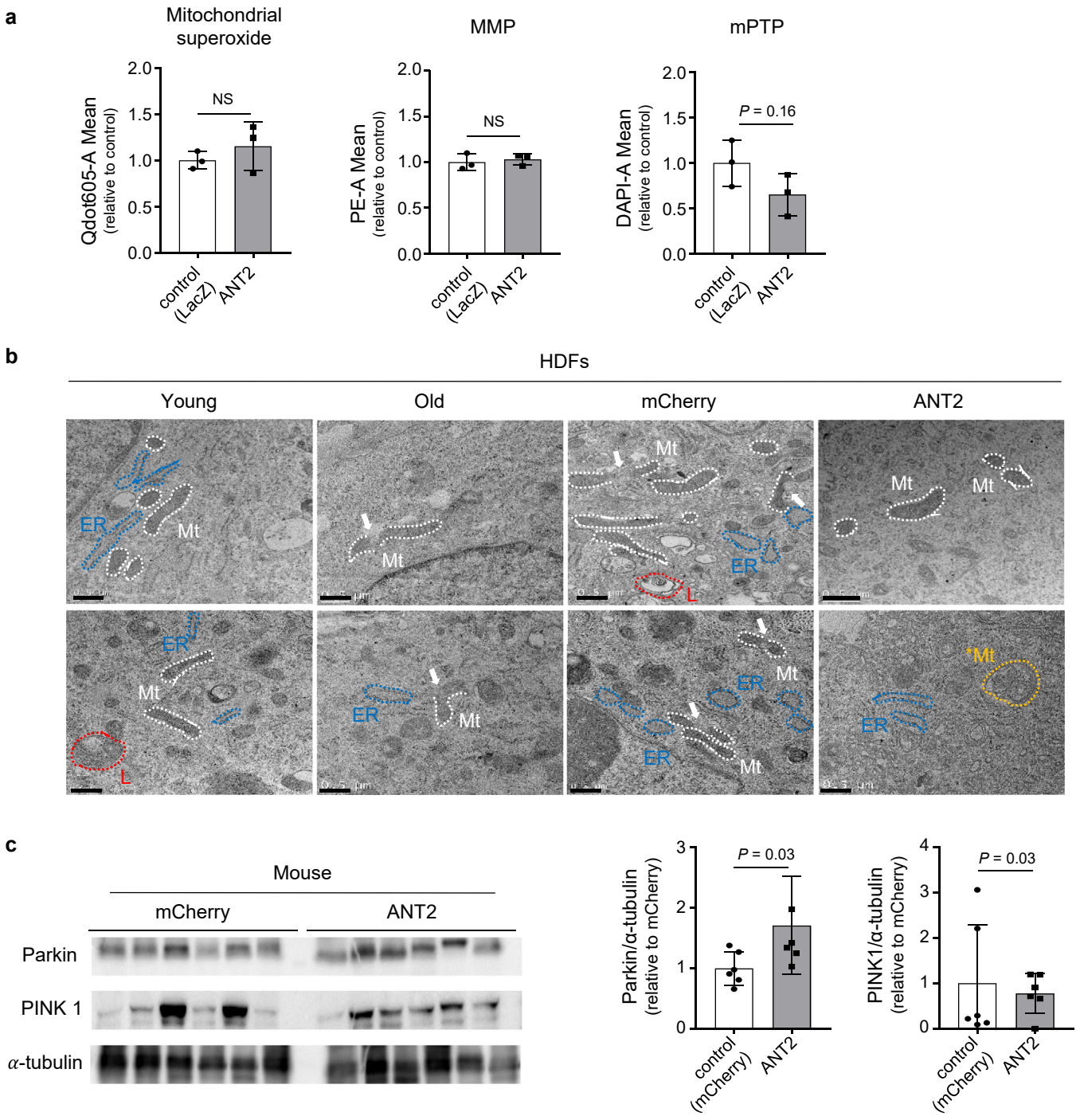

Supplementary Figure S7. Changes in mitochondrial morphology and properties by ANT2 overexpression in senescent HDFs. (**a**) Quantitative data for MitoSOX (mitochondrial ROS level), TMRM (MMP), and mPTP. The data are shown as the mean ± SD; n (biological replicate) = 3. (**b**) TEM images of HDFs. Damaged mitochondria (white arrows) and swollen ER (blue) were observed in the old and mCherry-OE (control) groups. On the other hand, intact mitochondria and narrow ER were observed in the young and ANT2-OE groups. Mt denotes mitochondria, *Mt denotes mitophagy, and L denotes lysosome. Bar = 0.5 μm. (**c**) Immunoblots and quantification of Parkin and PINK1 expression in mCherry-OE (control) and ANT2-OE mouse skin tissues. α-Tubulin was used for normalization. The data are shown as the mean ± SD; n (biological replicate) = 6. For statistical analyses in **a** and **c,** unpaired *t*-test was used. ANT2-OE, ANT2-overexpressing; ER, endoplasmic reticulum; HDF, human dermal fibroblast; mCherry-OE, mCherry-overexpressing; MMP, mitochondrial membrane potential; mPTP, mitochondrial permeability transition pore; NS, nonsignificant; TEM, transmission electron microscopy; TMRM, tetramethylrhodamine methyl ester.

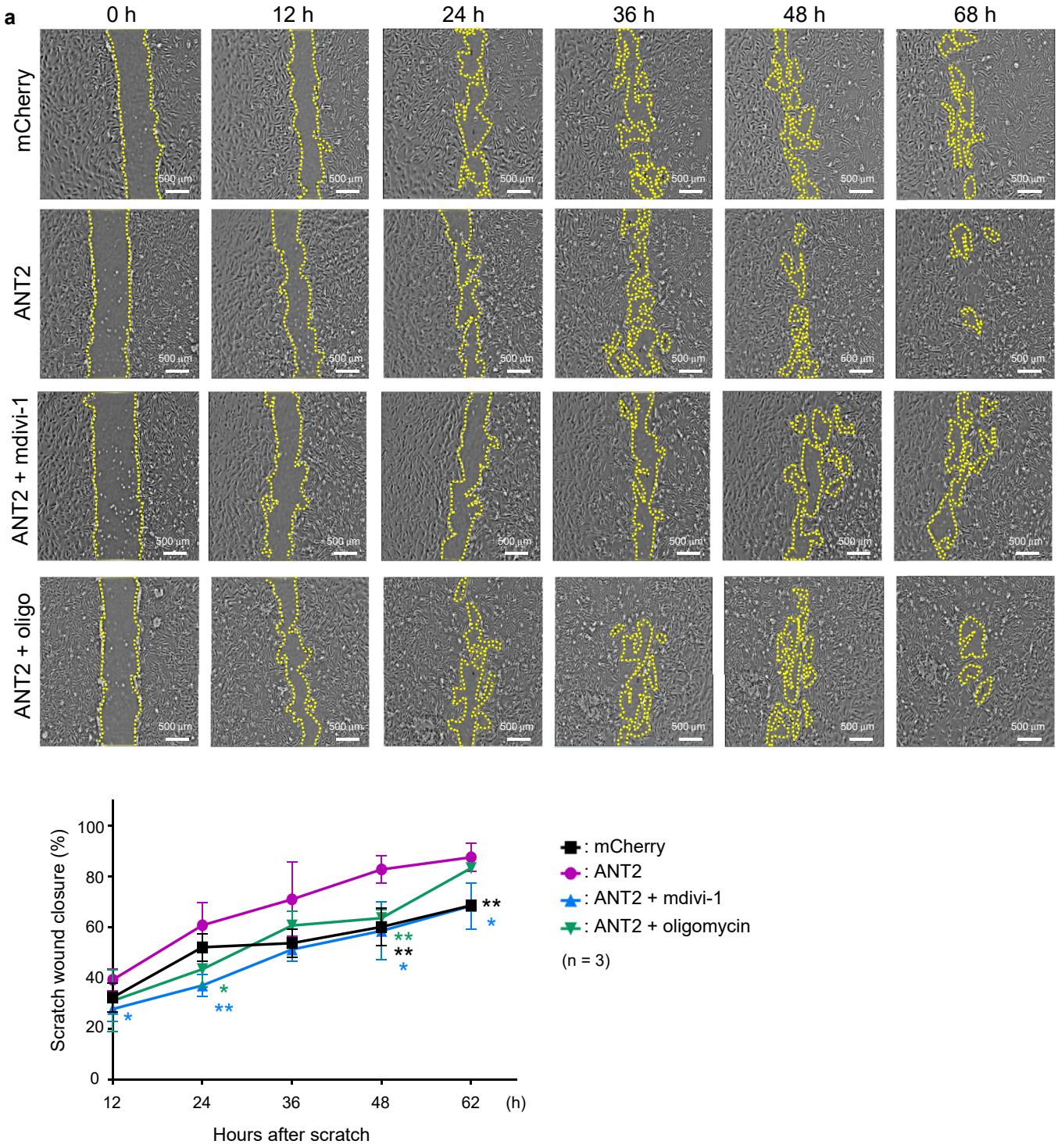

Supplementary Figure S8. Migration and proliferation capacity determined by mitophagy in ANT2-OE senescent cells. (**a**) A total of 10 μM mdivi-1 and 5 μM oligomycin were used for the experiments. Time-lapse images showing wound closure in senescent HDFs 0, 12, 24, 36, 48, and 68 h after scratch. The terminal cell migratory region is indicated by a yellow dotted line. Bar = 500 μm. The migration area was quantified with ImageJ software. The data are shown as the mean ± SD; n (biological replicate) = 3. (**b**) Images and quantification of EdU incorporation in four groups of senescent HDFs. The data are shown as the mean ± SD; n (view field) = 12. Significant data are represented as the mean ± SD. For statistical analyses in **a**, $*P \leq 0.05$ and $**P \leq 0.01$ as determined by multiple *t*-tests, and for those in **b**, $*P \leq 0.05$ and $****P \leq 0.0001$ as determined by unpaired *t*-tests. ANT2-OE, ANT2-overexpressing; EdU, 5-ethynyl-20-deoxyuridine; h, hour; HDF, human dermal fibroblast.

Supplementary Figure S8. Continued.

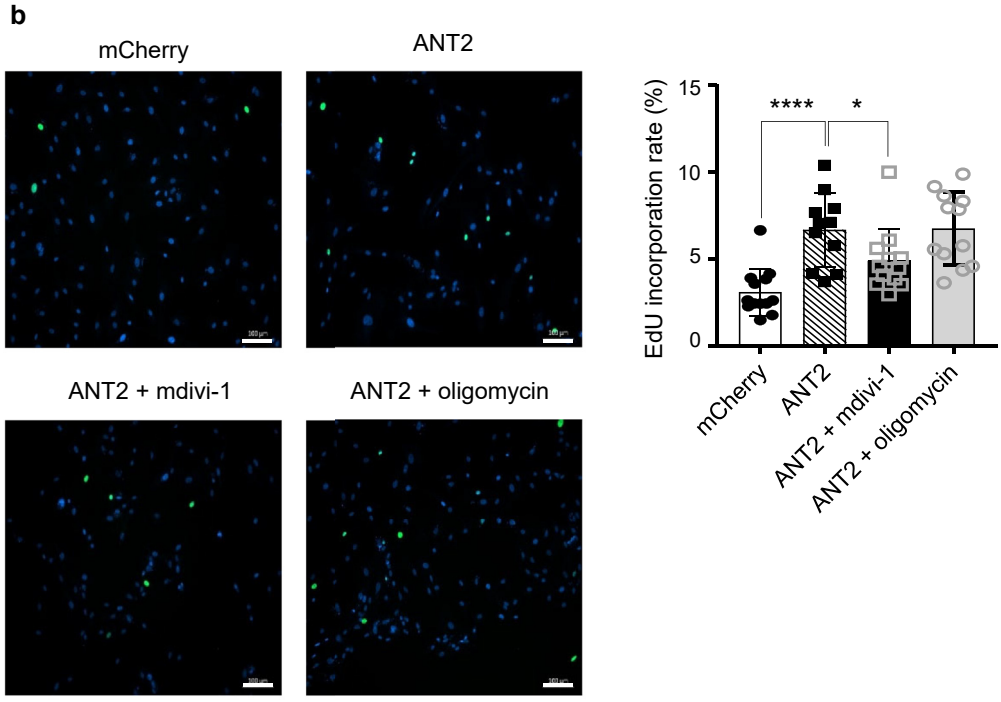

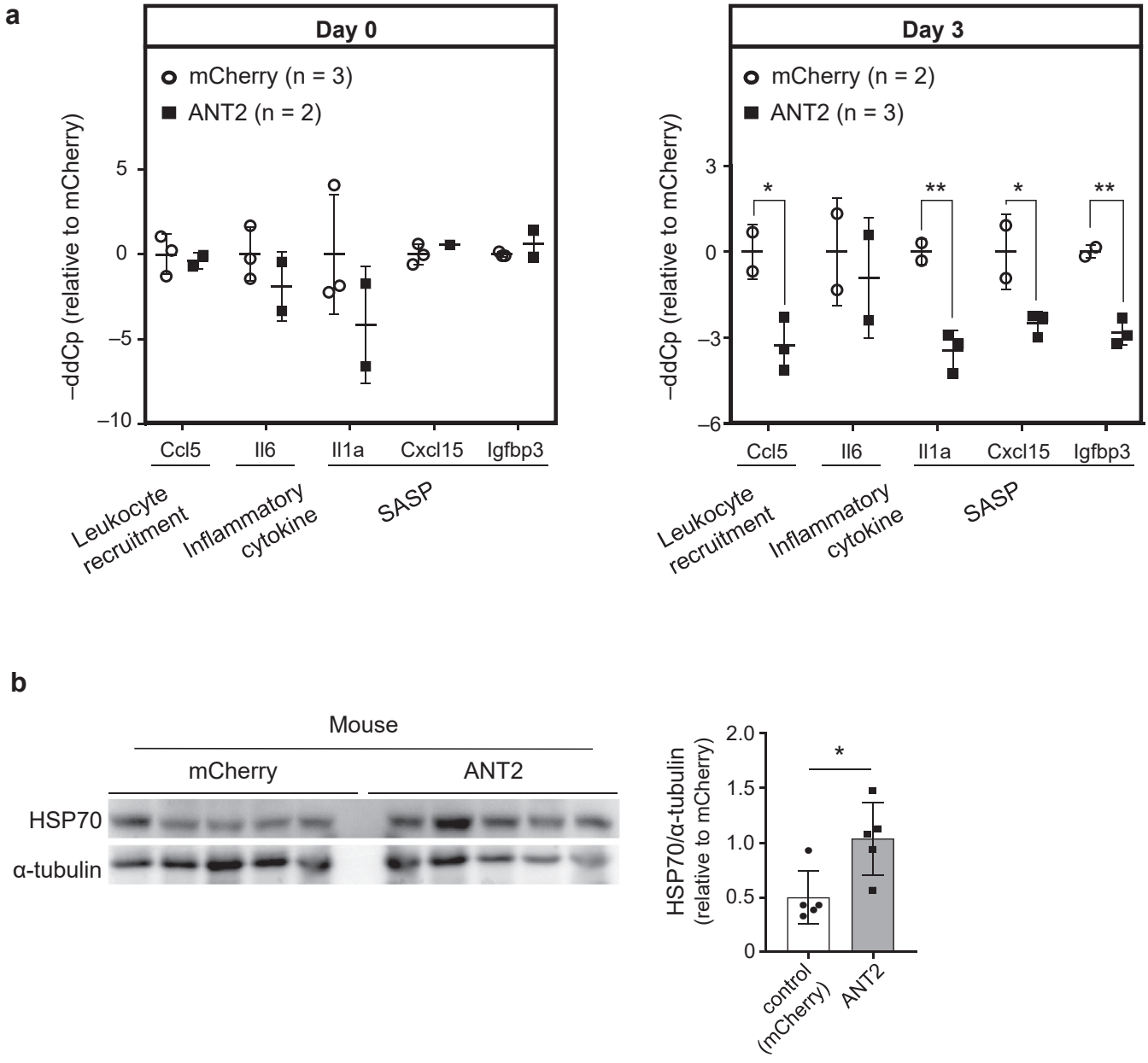

Supplementary Figure S9. Expression of proinflammatory cytokine genes at the inflammation phase in ANT2-overexpressed aged skin. (**a**) Expression of proinflammatory cytokine genes in the mCherry (control) group and ANT2 group of mouse skin on day 0 and day 3. The data are shown as the mean ± SD; n (biological replicate) = 2−3. (**b**) Immunoblots and quantification of HSP70 expression in mouse skin tissues of the mCherry (control) group and ANT2 group. α-Tubulin was used for normalization. The data are shown as the mean ± SD; n (biological replicate) = 5. For statistical analysis in **a** and **b**, $*P \leq 0.05$ and $**P \leq 0.01$ as determined by unpaired *t*-tests.

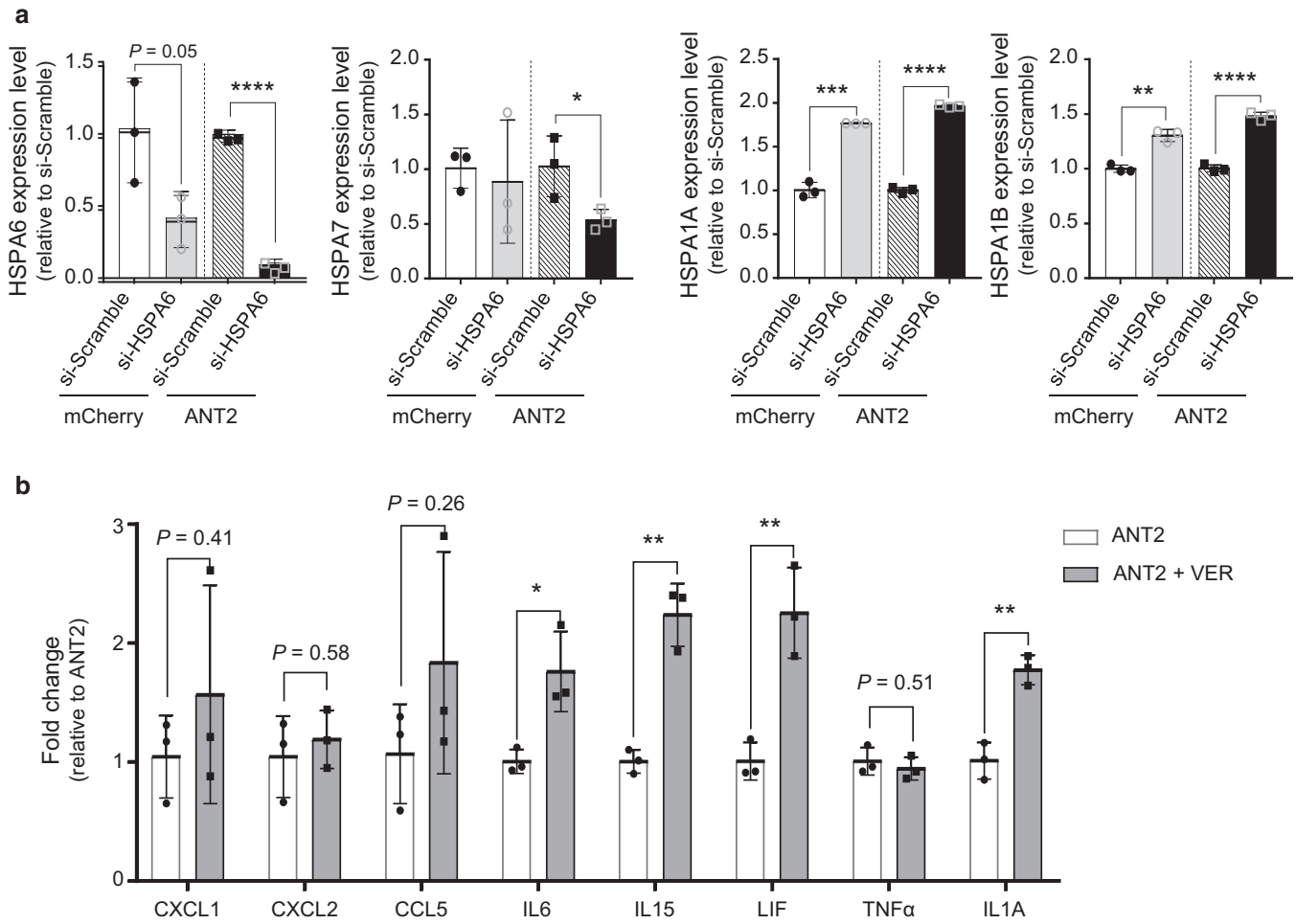

Supplementary Figure S10. Expression of proinflammatory cytokine gene after HSP70 inhibition in ANT2-OE senescent HDFs. (**a**) The expression of *HSP70* family genes after *HSPA6* knockdown using siRNA in mCherry-OE (control) and ANT2-OE senescent HDFs. The data are shown as the mean ± SD; n (biological replicate) = 3. (**b**) The expression of proinflammatory cytokine genes after VER-155008, an HSP70 inhibitor, was added to mCherry-OE (control) and ANT2-OE senescent HDFs. The data are shown as the mean ± SD; n (biological replicate) = 3−4. For statistical analysis in **a** and **b**, $*P \leq 0.05$, $**P \leq 0.01$, $***P \leq 0.001$, and $****P \leq 0.0001$ as determined by unpaired *t*-test. si denotes siRNA. ANT2-OE, ANT2-overexpressing; HDF, human dermal fibroblast; mCherry-OE, mCherry-overexpressing; siRNA, short interfering RNA.

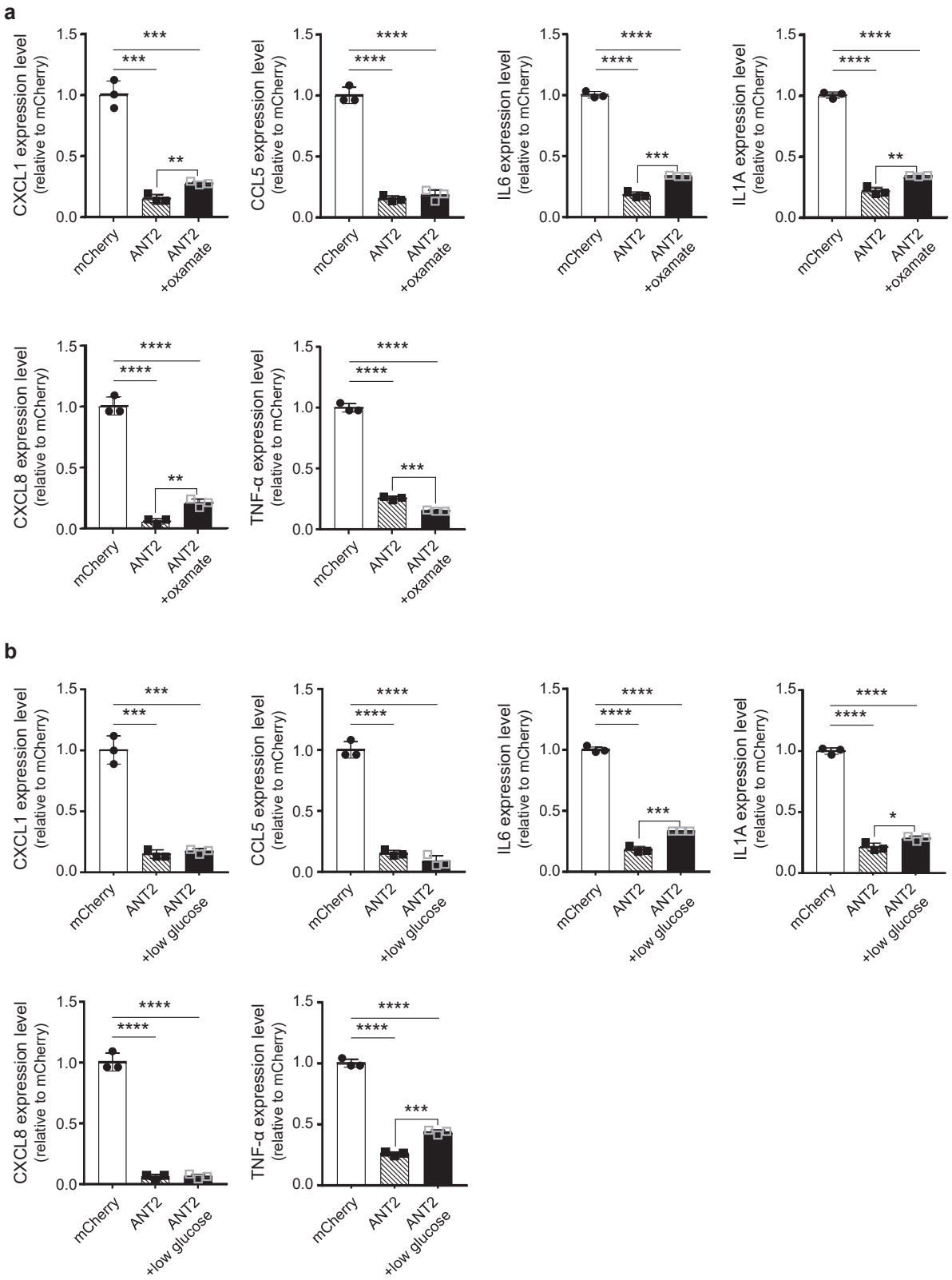

Supplementary Figure S11. Expression of proinflammatory cytokine gene after inhibition of glycolysis, oxidative phosphorylation, or mitophagy in ANT2-OE senescent HDFs. (**a**−**d**) The expression of proinflammatory cytokine genes after (**a**) 20 mM sodium oxamate treatment, (**b**) under low-glucose medium culture conditions, (**c**) 5 μM oligomycin treatment, and (**d**) 10 μM mdivi-1 treatment. The data are shown as the mean ± SD; n (biological replicate) = 3. For statistical analysis, $*P \leq 0.05$, $**P \leq 0.01$, $***P \leq 0.001$, and $****P \leq 0.0001$ as determined by unpaired *t*-test. ANT2-OE, ANT2-overexpressing; HDF, human dermal fibroblast.

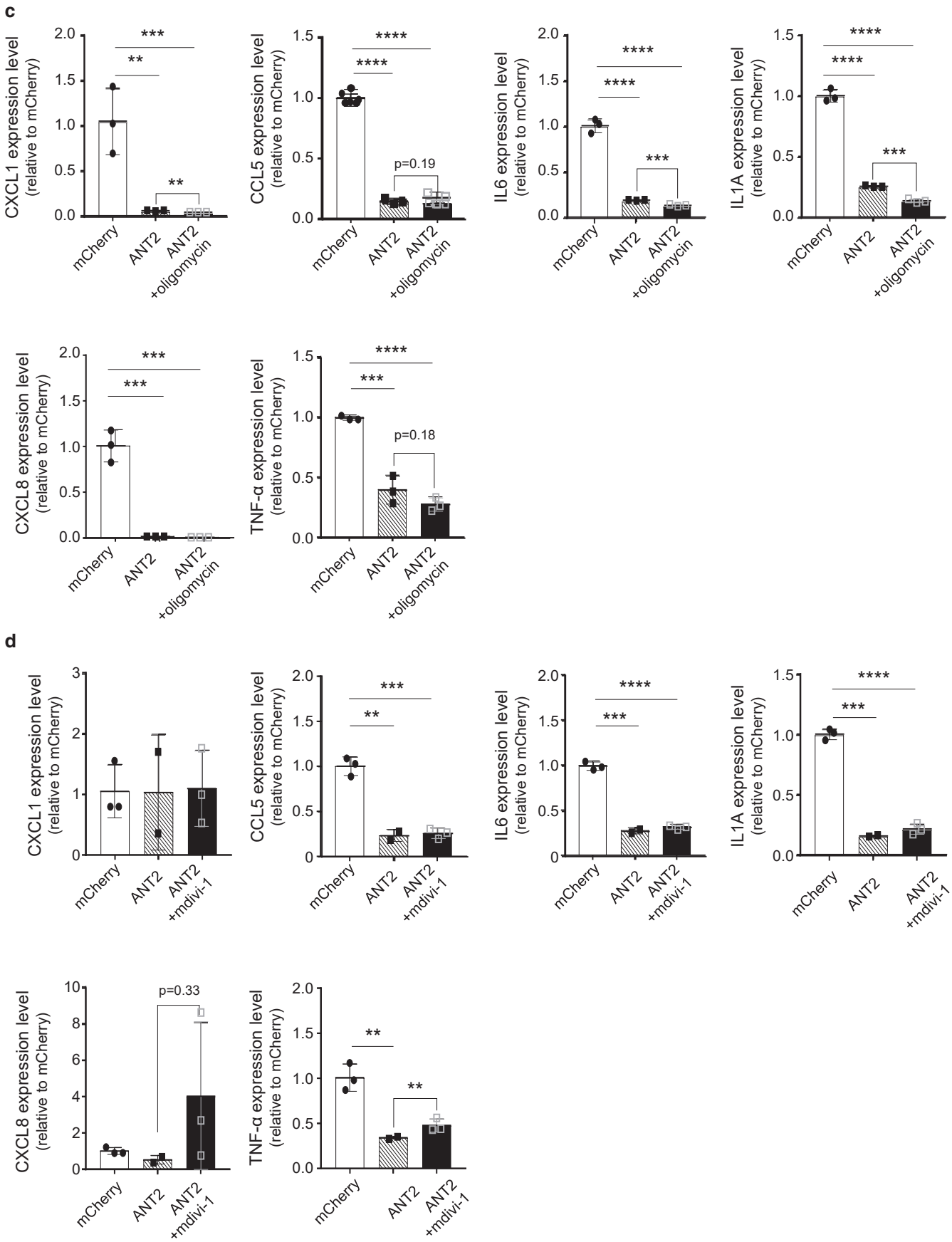

Supplementary Figure S11. Continued.